Geoscience Frontiers 16 (2025) 102003

Contents lists available at ScienceDirect

Geoscience Frontiers

journal homepage: www.elsevier.com/locate/gsf

Research Paper

Unravelling the geochemical and geochronological diversities of the pre-collisional magmatism: Implications for the subduction dynamics in the Kohistan island arc and Karakorum block, Pakistan

Matee Ullah [a,b,*], Urs Klötzli [a], Christian Rentenberger [c], Jiří Sláma [d], Muhammad Younas [e], Muhammad Khubab [f], Mohammad Goudarzi [a,g], Tanveer Ahmad [h]

[a] Department of Lithospheric Research, University of Vienna, Vienna, Austria
[b] Department of Geology, Khushal Khan Khattak University, Karak, Pakistan
[c] Physics of Nano Nanostructured Materials Laboratory, University of Vienna, Vienna, Austria
[d] Institute of Geology, Academy of Sciences of the Czech Republic, Prague, Czech Republic
[e] Department of Earth and Atmospheric Sciences, University of Houston, Houston, USA
[f] Department of Geology, University of Vienna, Vienna, Austria
[g] Department of Geology, Lorestan University, Iran
[h] Institute of Applied Geosciences, Karlsruhe Institute of Technology, Karlsruhe, Germany

ARTICLE INFO

Article history:
Received 6 June 2024
Revised 19 December 2024
Accepted 15 January 2025
Available online 23 January 2025
Handling Editor: S. Kwon

Keywords:
Subduction zones
Geochemistry
U-Pb geochronology
Transmission electron microscopy
Thermal modelling

ABSTRACT

The magmatic arcs in the north-west region of Pakistan comprises of numerous volcanic and plutonic bodies of different ages and compositions evolved during the subduction of the Neo- Tethys Ocean under the Eurasian supercontinent. This study focusses on the examination of the granitoids of the Kohistan batholith (a part of Kohistan-Ladakh Island Arc; KLIA) and the Khunjerab pluton, concentrating on their petrological traits, mineral chemistry, in-situ zircon U-Pb geochronology, and whole-rock major and trace element geochemistry. According to zircon U-Pb dating, the Kohistan batholith granitoid was emplaced around 91.7 ± 0.3 Ma, while zircons of the Khunjerab pluton yield ages of 106.4 ± 0.4 Ma and 106.4 ± 1.0 Ma. All the samples from both magmatic units have calcic to calc-alkaline ($Na_2O + K_2O$: 3.6–10.6 wt.% and SiO_2: 60–73 wt.%), metaluminous to peraluminous properties (Aluminum Saturation Index (ASI): 0.9–1.2). Notably, Nb, Ta, and Ti show depletion, while large ion lithophile elements like Cs, Rb, and K have been enriched. Additionally, we find that SiO_2 and P_2O_5 have a negative correlation while Rb and Th have a positive correlation, which confirm an I-type arc magmatism. Together with the published literature, TEM analysis, and thermal modelling, our zircon U-Pb results point to a period of continuous magmatic activity from the Late Jurassic to the Late Cretaceous (between 150 Ma and 91 Ma) in the Kohistan Island arc region while the Khunjerab pluton (part of Karakorum block/Eurasian plate) experienced widespread magmatism around 120 Ma to 106 Ma. With SiO_2 concentrations ranging from 67.5–73.3 wt.% and 60–71.4 wt.% and relatively low alkali ($Na_2O + K_2O$) contents between 3.6–10.6 wt.% and 5.1–7.4 wt.% in the Kohistan batholith and Khunjerab pluton respectively, showing clear signs of acidity. The whole rock as well as the mineral geochemical analysis and the elevated water contents (8–10 wt.% and 3.1–3.5 wt.%) inferred from amphibole and biotite chemistry respectively, indicates that the Kohistan batholith was most likely formed through partial melting of a (hydrous) magma originating from a more or less altered metasomatized mantle wedge. Likewise, the Khunjerab pluton whole rock geochemistry also indicates its origin through partial melting of magma originating from an altered metasomatized mantle wedge. This study also shows that both units are not only different in terms of the nature of magmatism but also in terms of their ages i.e., continental arc magmatism occurred in the Khunjerab (Karakoram) block in the middle Cretaceous (106 Ma) while island arc magmatism occurred on the Kohistan side in the late

* Corresponding author.
E-mail address: mateeu89@univie.ac.at (M. Ullah).

https://doi.org/10.1016/j.gsf.2025.102003

Cretaceous (91 Ma). Further, this study also investigate why multi-grain U-Pb zircon dating is necessary for studying magmatic rocks by using transmission electron microscopy.

1. Introduction

The chemical composition of the Earth has been significantly shaped by subduction zones, which are often compared to production centers of continental crust. In essence, they strongly contribute to the evolution of the continental crust by producing parental arc magmas and the plutonic rocks in the island/volcanic arcs derived thereof (Crawford and Searle, 1992; Tatsumi, 2005; Wu et al., 2016). The dynamics of the Earth's interior and global geochemical cycles are significantly affected by these recycling processes. Meanwhile, physical processes related to subduction, such as tectonic compression, are essential in establishing the thickness of the continental crust. In the Central Andes, for example, the continental crust is among the thickest in the world, measuring more than 70 km (Wigger et al., 1994; Giambiagi et al., 2012). This is thought to be the consequence of the South American Plate being compressed during the Neogene (Sheffels, 1990). Active subduction zones e.g., the Central Andes and the Himalayan-Indo-Eurasian orogeny have been the subject of much research on the interactions between subduction zone magmatism, tectonic compression, and crustal thickening (Wigger et al., 1994; Zhu et al., 2009; Giambiagi et al., 2012; Wu et al., 2016; Ali et al., 2024). Subduction-related magmatic rocks serve as "petrogenetic records" of paleo-tectonic events and provide important information about the dynamics of subduction zones and the evolution of deep crustal magma sources (Zhu et al., 2009; Giambiagi et al., 2012; Cao et al., 2016; Wu et al., 2016; Ali et al., 2024).

There were two subduction systems and associated island arcs existed between the Indian and Eurasian plates that have taken tectonic control over the Neo-Tethys Ocean during the Jurassic to Late Cretaceous period (Petterson, 2010; Jagoutz et al., 2019; Ali et al., 2024). The intra-oceanic Kohistan-Ladakh Island arc (KLIA) is thought to have formed from the Neo-Tethys Ocean subducting northward beneath the Meso-Tethys oceanic crust. At the same time, a similar overriding oceanic plate subducted northward beneath southern Eurasia, forming the Karakoram Arc (Petterson and Windley, 1991; Debon and Ali Khan, 1996; Jagoutz et al., 2019). The Indian Plate borders the Kohistan-Ladakh Island Arc (KLIA) to the south, and the Eurasian Plate borders it to the north.

The KLIA is an intra-oceanic arc. The dominant magmatic unit within this arc, the Kohistan batholith (KB), records a long period of magmatism that began about 154 Ma ago and ended in the Miocene (Schaltegger et al., 2002; Heuberger et al., 2007; Khan et al., 2009; Ali et al., 2024). The KLIA is situated between the Indian and Eurasian plates as a result of substantial tectonic activity that occurred during 154 Ma to 39 Ma. According to Petterson (2010), the arc indicates a significant addition of juvenile mantle material to the continental crust. The Matum-Das pluton, which was formed approximately 154 million years ago, is one of the oldest magmatic units in the KB (Schaltegger et al., 2002; Ali et al., 2024). The formation of the entire KLIA was aided by a number of units derived from the mantle and crust after this initial magmatism and is therefore important for the understanding of how the continental crust evolves here.

The southern side of the Eurasian i.e., the Karakoram region of Pakistan comprises of many irregularly distributed intrusive bodies of Mid to Late Cretaceous period (Fig. 1). Previous studies in this region have investigated the whole-rock major and trace element compositions and the zircon U-Pb geochronology of the Hunza plutonic complex, the Karakoram batholith, Khunjerab-Tirich Mir granite belt, and other granitic units (e.g., Crawford and Searle, 1992; Hildebrand et al., 2001; Ogasawara et al., 1992, 2008; Treloar et al., 1989). Based on the diverse geochemical signatures of the plutons, different lithologies and their various sources of magmas have been identified by Treloar et al. (1989), Crawford and Searle (1992), and Hildebrand et al. (2001). According to Hildebrand et al. (2001) and Ogasawara et al. (2008), the Rb-Sr whole-rock dating of the Tirich Mir granite suggests an age similar to that of the Khunjerab granodiorite i.e., the U-Pb dating of the Khunjerab granodiorite indicates the presence of continental arc magmatism along the southern margin of the Asian continent at approximately 110 Ma ago.

With regard to the Kohistan batholith granitoids and the Khunjerab pluton granitoids, this study reports new results on zircon U-Pb ages, the mineral chemistry, the whole-rock major and trace element data, and TEM analysis of dated zircon to investigate the nano scale geochemical processes that may alter the zircons and so their U-Pb ages. By combining our findings with previously gathered structural and geochemical data, this work presents a novel petrogenetic framework that clarifies subduction zone magmatism in both of these mentioned regions (Fig. 1). Our models further investigate the nature and the relationship between the two types of magmatism on either side of the KLIA and Karakoram block (Eurasian plate).

2. Geological background

The northern part of Pakistan consists of Himalaya ranges from south to north that includes the India plate, the KLIA, and the Karakoram block (southern part of the Eurasian plate). As shown in Fig. 1 (Searle et al., 1999), these segments are distinguished by geological features such as the Indus suture zone or Main Mantle Thrust (MMT), the Main Karakoram Thrust (MKT), the Shyok Suture or the Karakoram-Kohistan Suture. The KLIA represents a complete vertical slice extending from Earth's mantle to rocks on top of the crust. It collided with the Eurasian (Karakoram) plate approximately 75–102 Ma ago, and changed into an Andean-like margin (Khan et al., 2009; Bosch et al., 2011). The southern side of KLIA had experienced a continental collision with the Indian Plate about 55–50 Ma ago (Petterson and Windley, 1985; Khan et al., 2009). The rocks have thrusts and folds that are sharply inclined and tilt northward as a result of these collisions (Petterson and Windley, 1985). The arc is divided into seven east–west trending geological units that span Jurassic to Oligocene ages. These units are the Yasin detrital series, Chalt Volcanics, Kohistan batholith, Jaglot group, Chilas Complex, Kamila Amphibolites, and Jijal-Sapat Complex, going from north to south (Heuberger et al., 2007; Khan et al., 2009; Jagoutz et al., 2019). It is believed that the Jijal-Sapat and Kamila Amphibolites form the arc's base (Khan et al., 2009; Jagoutz et al., 2019). The southern part of the arc is divided from the Kohistan batholith by the Chilas Complex (age is ~ 83–86 Ma), a unit of mafic to ultramafic rocks (gabbronorites) that represents the root zone of magma chamber for the KLIA.

An integral part of the KLIA, the Kohistan batholith is composed of distinct plutons, stocks, dykes, and sills of calc-alkaline gabbros,

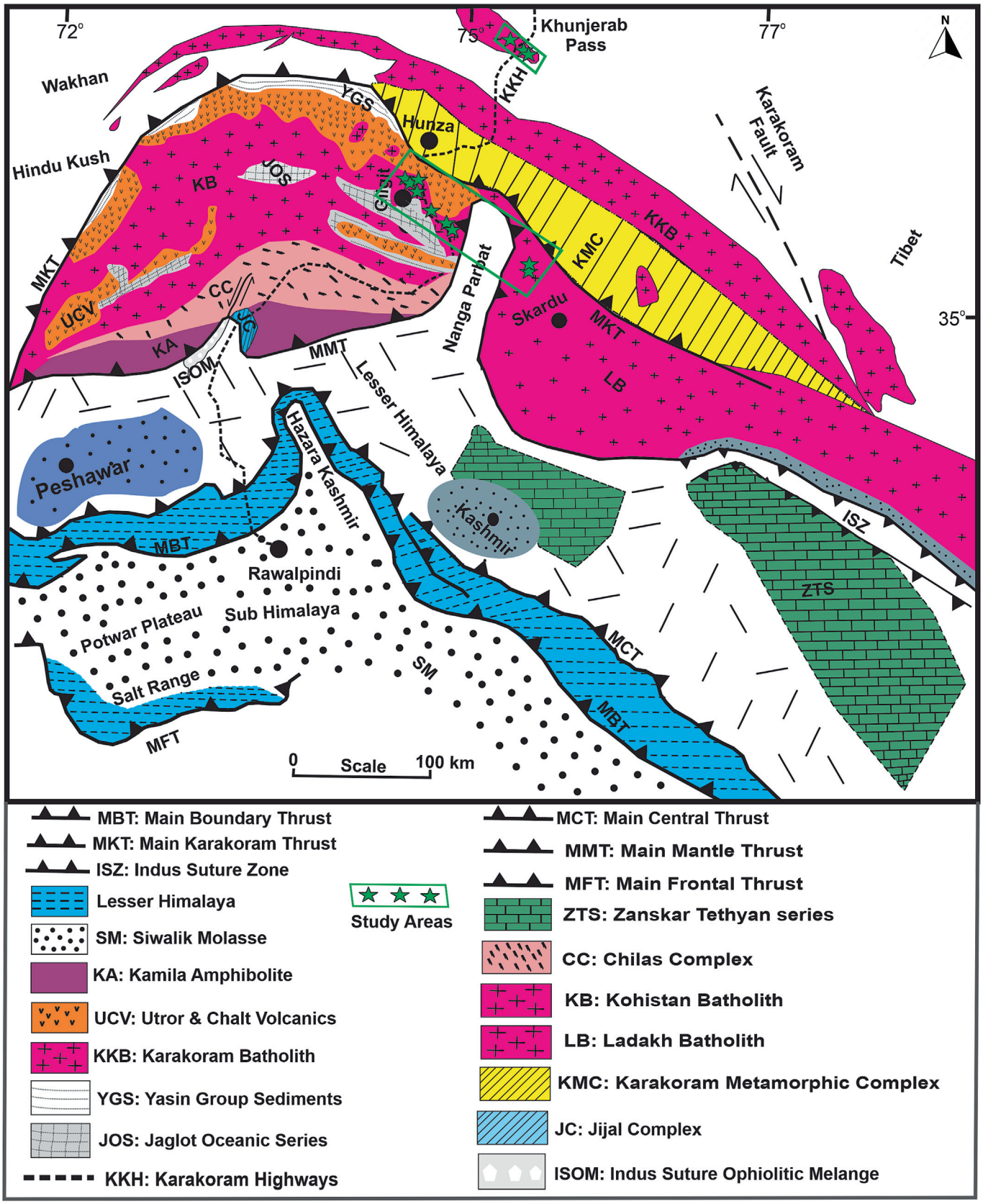

Fig.1. Geological map of northern Pakistan showing the spatial extent of different geological units along with the major magmatism in the Kohistan-Ladakh and Karakorum and Khunjerab area (Searle et al., 1999). The study areas are enclosed in the blue (Kohistan Batholith; KB) and green (Khunjerab pluton; KP) rectangles while the green stars represent the sample locations.

diorites, granites, and tonalites (Heuberger et al., 2007; Khan et al., 2009; Jagoutz et al., 2009). According to the emplacement ages and the existence or lack of gneissic fabrics, the magmatic rocks of the Kohistan batholith are divided into three stages (Petterson and Windley, 1991). Approximately one-third of the plutons in the Kohistan batholith are stage 1 rocks, which have gneissic foliation and a bimodal composition of high-K to low-K gabbros and diorites that are deformed. The intrusions in stages 2 and 3 are thought to have formed after the collision because they do not show/possess sub-solidus deformation fabrics. The Andean-type stage 2 plutons are composed of gabbros cut by diorites and granites (60–40 Ma) and gabbro-diorites (85 Ma). Stage 3 rocks are post-collisional granites (34–26 Ma) cross-cut by aplitic-pegmatites and leucogranite sheets; they demarcate the last stage of the KB's magmatism (Petterson and Windley, 1991; Petterson, 2010). These Kohistan batholith intrusive bodies have a calc-alkaline affinity suggests significant magmatic differentiation and interaction between mantle-generated magmas and pre-existing crust (Petterson and Windley, 1991; Argles et al., 2003).

Before the Late Cretaceous collision of the KLIA with Asia (102 Ma and 85 Ma, as per $^{40}Ar/^{39}Ar$ and K-Ar dating; Treloar et al., 1989), the Karakoram block was located at the southern edge of the Asian continent. In the Early Cretaceous, continental arc magmatism formed in the Karakoram block as a result of northward subduction of oceanic plate under Asia. Within the Karakoram block, the Karakoram batholith is one of the dominant granitic bodies. In the north of the Karakoram batholith there are smaller granitic intrusions such as the Khunjerab-Tirich Mir granite belt, the Khunjerab pluton, and the Hunza plutonic complex. The Karakoram batholith (85–102 Ma; Treloar et al., 1989) probably formed after the first major phase of plutonic activity in Kohistan and Ladakh (154 Ma to ca. 107 Ma ago; Schaltegger et al., 2002; Heuberger et al., 2007). Kohistan and Ladakh pluton activity are thought to have been approximately concurrent with the first intrusive phase of the Hunza plutonic complex in the Karakoram (Petterson and Windley, 1985; Crawford and Searle, 1992). The majority of the pre-collisional (before $\sim$ 50 Ma; Khan et al., 2009) plutonic activity was composed of granodiorite intrusions, though some compositional variation ranging from gabbro to leucogranite also exist. The existence of continental arc magmatism around 110 Ma along the southern periphery of the Asian (Eurasian) continent is suggested by U-Pb dating of the Khunjerab granodiorite and the Rb-Sr whole rock dating of the Tirich Mir granite belt (Ogasawara et al., 2008). Although the initial $^{87}Sr/^{86}Sr$ ratios were low and resembled those of a typical Andes type subduction related granite (Petterson and Windley, 1985). The isotopic analyses of Honegger et al. (1982) shows some degree of crustal contamination. The calcic-alkaline I-type granitoid intrusive units found in the Karakoram area are believed to have developed as a result of advanced assimilation-fractional crystallization of mantle-derived basaltic magmas (Crawford and Searle, 1992; Ogasawara et al., 2008; Petterson and Windley, 1985). After the Indian and Asian plates collided to form the Indus suture/MMT approximately 50 Myr ago, more acidic magmas, such as monzogranitic and leucogranitic dykes and plutons, began to be intruded in both the Kohistan-Ladakh and the Karakoram region (Crawford and Searle, 1992; Ogasawara et al., 2008; Petterson and Windley, 1985). The Karakoram batholith divides two different regions within the Karakoram region itself. The Karakoram metamorphic complex located between the batholith and the Shyok suture zone (SSZ) and the main Karakoram thrust (MKT), which is closely aligned with the SSZ's path, defines the complex's southern border (Fig. 1). The sedimentary deposits of the Carboniferous to Jurassic periods, which are part of the northern sedimentary terrain on the northern side of the Karakoram batholith, exhibit evidence of localized low-grade metamorphism (Crawford and Searle, 1992; Searle et al., 1999).

3. Analytical methods

3.1. Electron probe microanalysis (EPMA)

Using a CAMECA SX Five EPMA at the Department of Lithospheric Research, University of Vienna; Austria, major-element concentrations in the minerals (amphibole, biotite, and feldspar) of granitoids from the Kohistan Batholith and the Khunjerab pluton samples were investigated. This EPMA is equipped with five crystal spectrometers and a field emission cathode for highly accurate spatially resolved elemental analysis on polished solid surfaces. For quick semi-quantitative elemental analysis, the instrument also has an energy dispersive analysis system (EDX). A beam current of 5 – 15 nA and an accelerating voltage of 15 kV were used for the analysis. Natural and artificial minerals with known compositions were used as standards to guarantee accuracy. Standard ZAF data corrections were applied to determine oxide-form elemental concentrations.

3.2. LA–ICP-MS U–Pb dating of zircon

To determine the zircon U-Pb ages, three samples were selected (one sample (KB1) from the Kohistan batholith; two samples (KP1, KP4) from Khunjerab pluton). Zircon was separated at the Department of Lithospheric Research, University of Vienna, by gravity and heavy liquid separation. This separation was followed by hand-picking of various grains and then mounting them in epoxy resin followed by subsequent polishing. The mounts were carbon-coated and zircon crystals were further characterized by using a FEI Inspect S scanning electron microscope, equipped with a 50 mm^2 Oxford detector. Images with cathodoluminescence and secondary electrons were taken to visualize the zoning of the zircons. These cathodoluminescence and secondary electrons images allow the determination of the desired areas to be measured. For in-situ laser ablation ICP-MS U-Pb age dating, the mounts were analysed at the Institute of Geology of the Czech Academy of Sciences in Prague (Czech Republic), where a Thermo Scientific double-focusing magnetic sector field Element 2 HR-ICP-MS coupled to a 193 nm ArF excimer laser (Teledyne Cetac Analyte Excite laser) was used. The laser conditions were set to a repetition rate of 5 Hz, 25 μm spot size and fluence of 3.53 J/cm^2. Before the introduction into the ICP, the He-carrier gas was flushed through the two-volume ablation cell at a flow rate of 0.89 L/min and mixed with 0.661 L/min Ar and 0.004 L/min N. All gases and aerosols are mixed in the in-house glass signal homogenizer (design of Tunheng and Hirata, 2004) right before entering the torch. The measurement of U, Th and Pb signals from the ablated zircon was for 35 s. Typical acquisitions consisted of 15 s measurement of blank followed by measurement of U, Th and Pb signals from the ablated zircon for another 35 s. The accuracy of 238 mass measured in "both" mode is dependent on the correctly determined ACF (Analog Correction Factor). In order to correct for this variability, the data are pre-processed using a Python routine for decoding the Thermo Element ICPMS data files (Hartman et al., 2017) and an in-house Excel macro. As a result, the intensities of 238 are left unchanged if measured in a counting mode and recalculated from ^{235}U intensities (using the natural $^{238}U/^{235}U$ of 137.818). In all cases the ^{238}U was acquired in analogue mode, thus eliminating the non-linearity between pulse counting and analogue detecting modes. Then the Iolite v3.5 software (Paton et al., 2011) with the Vizual Age utility (Petrus and Kamber, 2012) was used for data normalisation, uncertainty propagation and export. Blank

intensities and instrumental bias were interpolated using an automatic spline function. Down-hole inter-element fractionation (LIEF) was corrected using an exponential function. LIEF correction assumes reference material and samples behave identically. Full details of the methodology can be found in Paton et al. (2011). No common Pb correction was applied to the data. The ages are quoted at 2σ absolute, propagation is by quadratic addition. The reproducibility and age uncertainty of reference material are propagated where appropriate following the recommendation of Horstwood et al. (2016). As primary reference material, Plešovice (Sláma et al., 2008) was used, whereas the reference materials GJ-1 (Jackson et al., 2004) and 91500 (Wiedenbeck et al., 1995) were used as secondaries and for validation and are periodically analysed during the measurement for quality control. The mean Concordia age values were 606 ± 3 Ma (2σ) for GJ-1 and 1063 ± 5 Ma (2σ) for 91500, obtained from analyses. Final ages were calculated using IsoplotR of Vermeesch (2018) and Noda (2017).

3.3. ICP-MS whole-rock geochemistry

Major and trace element analysis was performed on twelve samples, three from Khunjerab pluton and nine from the Kohistan batholith. Fresh whole-rock specimens were first broken into small pieces and thoroughly cleaned with distilled water that had been diluted with 5% HNO_3. This was followed by a rinse using only distilled water. The samples were then dried and closely examined to make sure there wasn't any obvious contamination. An agate ring mill was used to crush and grind the chosen samples, and the resulting powders were analyzed for major and trace elements. A Leeman Prodigy inductively coupled plasma-optical emission mass spectroscopy system with high-dispersion Echelle optics was used to analyze the major elemental compositions of the entire rock specimens. One gram of the sample was heated to 1000 degrees Celsius for several hours, cooled in a desiccator, and then weighed again to calculate the loss on ignition. Major element analytical uncertainties were found to be less than 5%. An Agilent-7500a Quadrupole-ICP-MS was used for whole rock trace element analysis.

3.4. FIB and transmission electron microscopy

Focussed Ion Beam (FIB) milling was used to create two TEM foils (12 μm × 6 μm × 0.045 μm) to investigate the structural properties of zircon. Selected regions measuring 20 μm × 2 μm were covered with a 1.5 μm layer of Pt to shield them from the Ga-ion beam during FIB milling. A beam current of 45 nA and an acceleration voltage of 30 kV were used to sputter the foils laterally. The raw foils were placed on a half-moon-shaped copper grid and thinned to a thickness of about 45–58 nm using different beam currents between 1 nA and 0.01 nA at a voltage of 30 kV. The last polishing was carried out at 27 pA and 2 kV. The detailed procedure for the sample preparation is given in Wirth (2009). The TEM analysis are performed using a FEI Titan 80–300 at the Department of Physics of Nanostructured materials, University of Vienna, Austria. Fast Fourier Transforms (FFT) were used to compute diffraction patterns from high-resolution electron microscopy images (HREM). Crystallographic parameters such as Miller indices (*hkl*), angles between neighboring planes, and the dhkl spacing were used for phase identification; an angular error of less than 1° was required for a clear identification. In FFT measurements, the angular error was less than 0.5. High-angle annular dark-field (HAADF) images were taken at a camera length of 75 mm, mainly Z-contrast images. The contrast was reversed in the bright field (BF) images, where the same phases appeared dark due to strong electron absorption by high atomic number phases or lower density materials. In HAADF Z-contrast images, bright areas indicated a chemical composition dominated by high atomic numbers (e.g., U, Th, or Pb) or higher density.

4. Results

4.1. Petrographic investigations

Both field and laboratory work reveal that the Kohistan batholith and Khunjerab plutons share many similarities in their respective compositions but at the same time show different textures. The Kohistan batholith granitoids (i.e., in the representative samples KB1, KB10, and KB13 were considered) are mostly medium to coarse grained with quartz, plagioclase, K-feldspar, biotite, chlorite, amphibole (Fig. 2a-d) and accessory minerals like epidote, zircon, apatite, monazite and allanite. In samples from Khunjerab pluton (i.e., samples KP1 and KP5) the same minerals are present with optically different level of alteration and deformation as compared to that of Kohistan batholith (Fig. 2e-h).

In samples KB1, KB10, and KB13, the finer material (ground mass) surrounds the larger subhedral to euhedral plagioclase and K-feldspar grains (Fig. 2a-d). The samples of Kohistan batholith are plutonic, medium to coarse grain in nature and have phaneritic, poikilitic, and inequigranular texture. In these samples, the majority of the rock's ground material, or groundmass, is composed of abundant quartz, with considerable amounts of biotite, chlorite, and other minerals like amphibole and epidote which are present in small amounts (Fig. 2a-d). The samples of both areas were variably altered as indicated by the chloritized biotite and the sericitized plagioclase (i.e., most plagioclase in Khunjerab pluton samples: Fig. 2).

In samples KP1 and KP5, the plagioclase grains are found as large subhedral to euhedral crystals within a finer-grained surrounding material (mostly quartz). The grains display albite polysynthetic and Carlsbad twinning (Fig. 2e-h). Many of these grains display evidence of alteration into epidote (Fig. 2e). All the samples of Khunjerab pluton are medium to coarse grain also display poikilitic, inequigranular, and phaneritic texture. Twin layers within the plagioclase grains exhibit patchy and undulose extinction, kinking of twin lamellae, and intragrain deformation. The most common mafic mineral found in these samples is biotite, which is found as aligned flakes showing strong brown to reddish brown and greenish pleochroism (Fig. 2g). Some of these biotite flakes may have a deep brown hue from iron oxidation and leaching, and they frequently have inclusions of other minerals like epidote, allanite, zircon, and apatite. In samples of both units, chlorite is found around the edges of the biotite flakes as shown in Fig. 2g.

In samples from both magmatic units, the large subhedral crystals of K-feldspar occur in a fine-grained quartz matrix with both orthoclase and microcline varieties. The majority of grains have unique twinning patterns; orthoclase has simple twinning, while microcline has Tartan or cross-hatched twinning (Fig. 2). Due to alteration processes, some K-feldspar grains appear relatively pristine, while others are cloudy. Some of the grains have broken apart due to brittle deformation, the resulting fractures being filled with fine-grained quartz and feldspar that has recrystallized, effectively healing the cracks.

Many of the investigated samples contain minor to trace amounts of amphibole; the occurrence of it is noticeably higher in samples (KP1 and KP5; Fig. 2e-f) from Khunjerab pluton than in those from the representative samples of Kohistan batholith sections (KB1, KB10 and KB13; Fig. 2a). Amphibole crystals are anhedral to subhedral and are typically found in clusters, mostly in relation to biotite flakes. Garnet is observed mostly in association

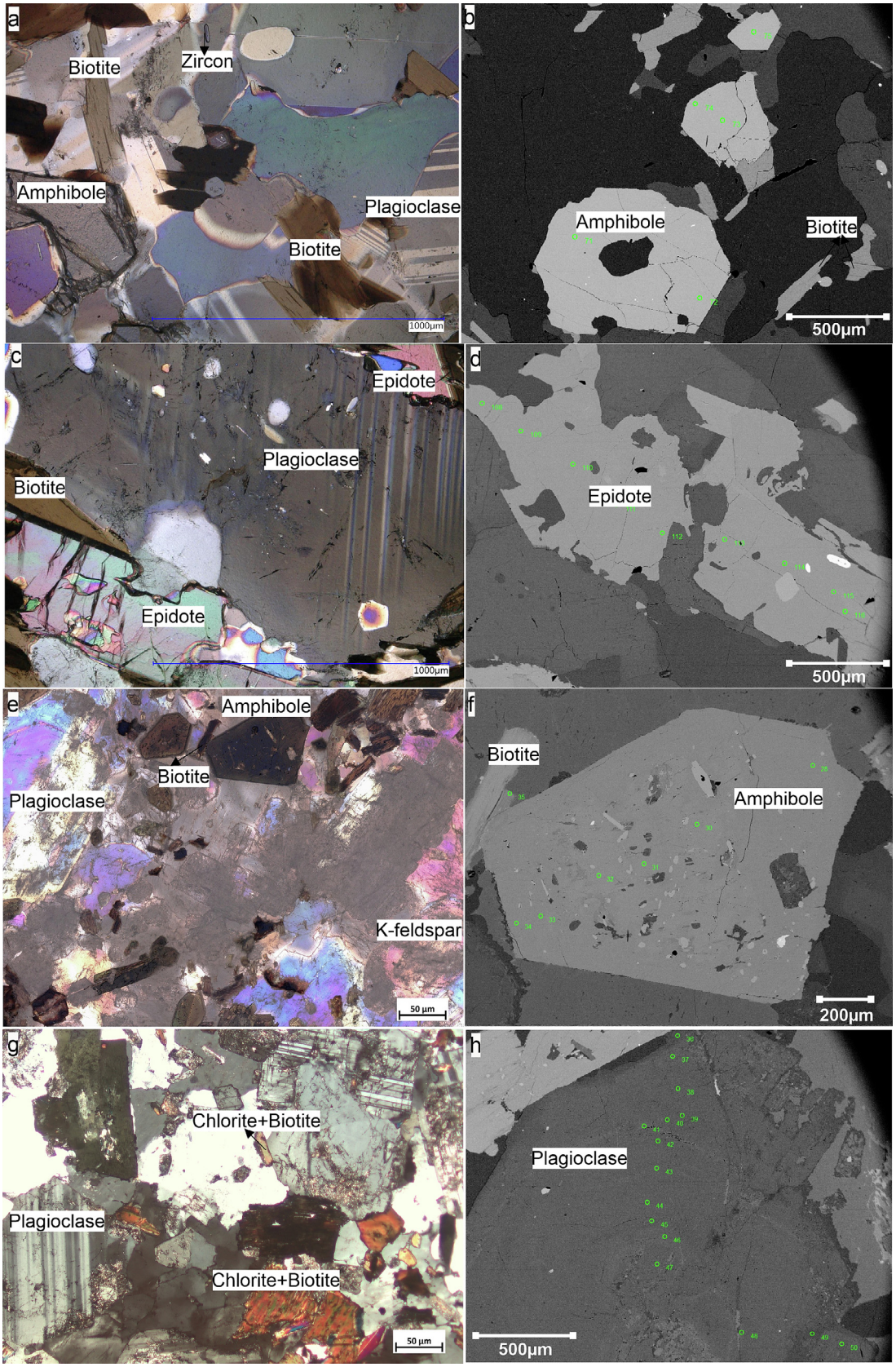

Fig.2. Optical and SEM photomicrographs of the petrographic features in the samples from the Kohistan batholith (a-d) and the Khunjerab pluton (e-h). (a) The amphibole, plagioclase twinning, zircon and biotite flakes; (b) an amphibole grain under a scanning electron microscope reflecting brighter relief than the surroundings; (c-d) a deformed and highly fractured epidote; (e) an image of plagioclase feldspar, K-feldspar and biotite; (f) grains of amphibole under scanning electron microscopy; (g) an image of chloritized biotite; (h) a euhedral plagioclase crystal.

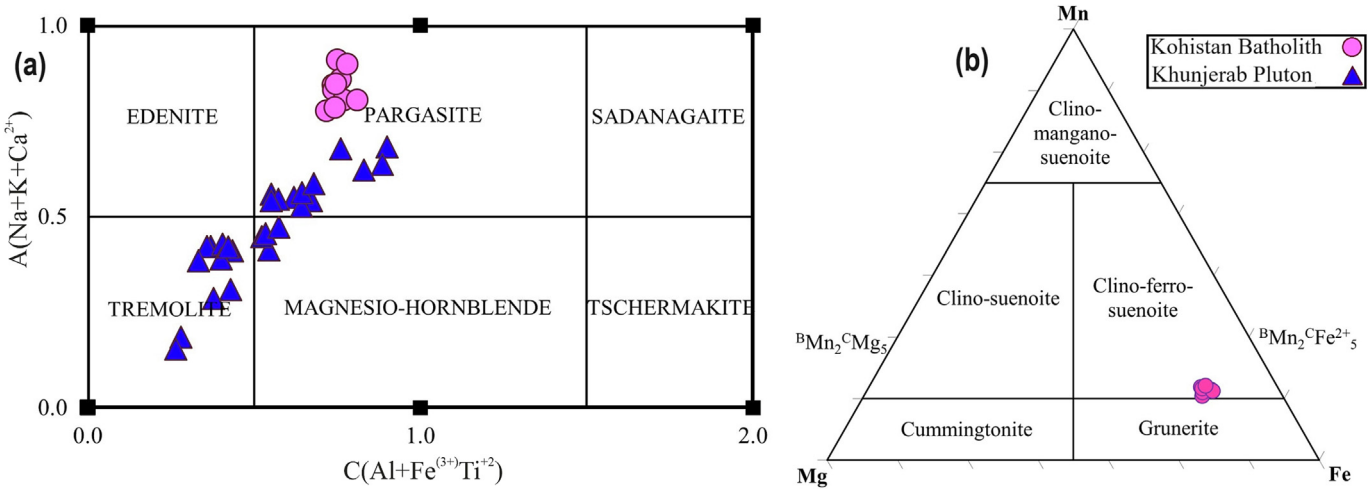

Fig.3. (a-b) Chemical composition of the analysed amphibole in both pre-collision magmatic units.

with biotite. Occasionally, trace quantities of zircons are observed as prismatic crystals with high relief (Fig. 2a).

4.2. Mineral chemistry

The chemical composition of amphibole, biotite, K-feldspar and plagioclase has been determined using EPMA (Supplementary Data Table S1–S3). Five samples, three samples (KB1; granodiorite, KB10; granite, and KB13; granodiorite) from Kohistan batholith and two samples (KP1; diorite, and KP5; granodiorite), were chosen to represent the entire spectrum (intermediate-felsic) of the petrographic variation of both areas.

Eleven out of twenty of the analysed amphiboles from the Kohistan batholith (from samples KB10 and KB13) fall within the calcic sub-groups (Fig. 3a), classifying as pargasite, while the remaining nine represent clino-ferro-suenoite (Fig. 3b). Amphibole in the samples (KP1 and KP5) of the Khunjerab pluton are classified as tremolite and pargasite (blue filled triangle points in Fig. 3a).

The biotite analysis shows a molar Fe/(Fe + Mg) ratio of 0.50–0.53 (Supplementary Data Table S2A) in Kohistan batholith (samples KB1, KB10, and KB13) and 0.37–0.58 (Supplementary Data Table S2B) in sample (KP5) of Khunjerab pluton, respectively. All the biotite composition in both regions correspond to annite-siderophyllite (Fig. 4a-c) according to Tischendorf et al. (1997),

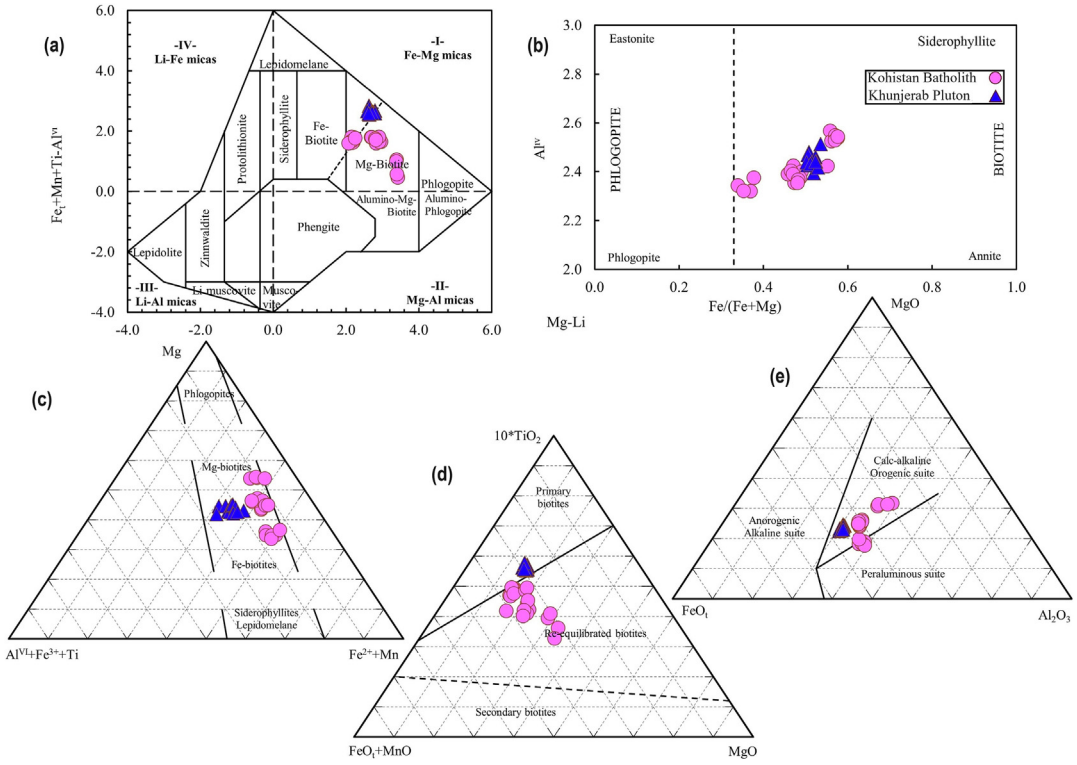

Fig.4. (a-e) Chemical composition and classification of the analysed biotite in the Kohistan batholith and Khunjerab pluton, while (d-e) show the tectonic classification of the same biotite.

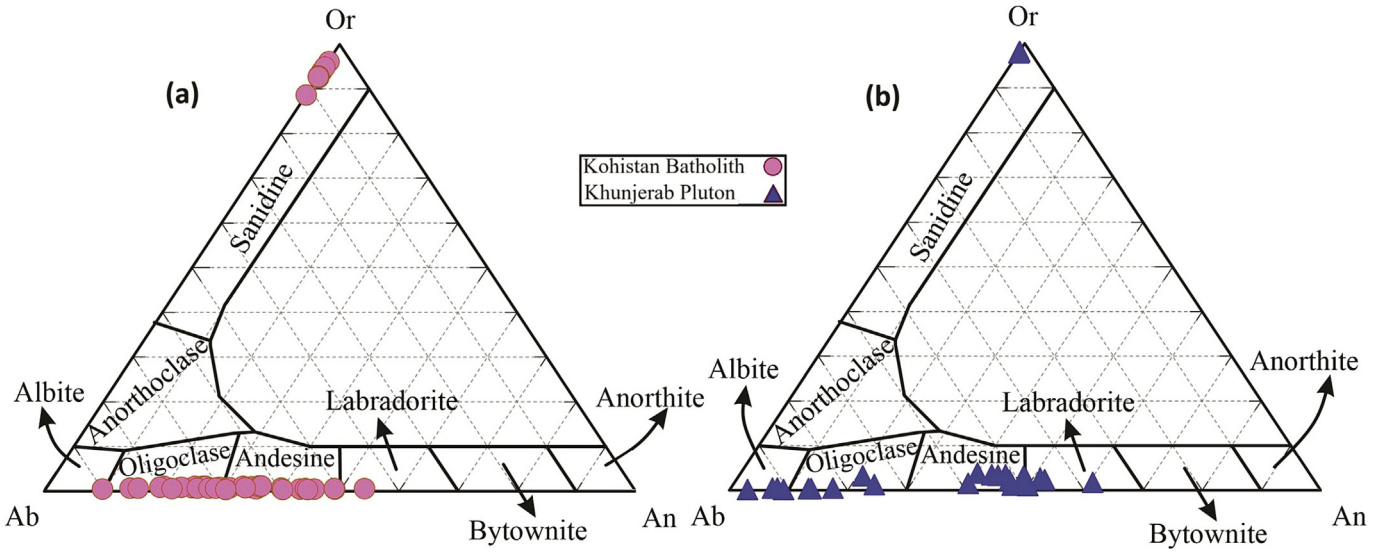

Fig.5. Geochemistry and chemical classification of the plagioclase-feldspar and K-feldspar from (a) Kohistan batholith, (b) from Khunjerab pluton.

Fosterm (1960), Nachit et al. (2005), and Abdel-Rahman (1994) nomenclatures. There are trace amounts of titanium (0.50–0.54 apfu) in the samples of Kohistan batholith which is slightly higher than the amount (0.19–0.36 apfu) present in Khunjerab pluton. Relative to Mg-Al^{IV} + Fe^{+3} + Ti-Fe^{+2} + Mn, 10×TiO_2-FeO_t + MnO-MgO and MgO–FeO_t–Al_2O_3 ternary discrimination diagrams, biotite compositions from the Kohistan batholith primarily vary from Fe-rich to more Mg-rich biotite, lying within the re-equilibrated an-orogenic field and calc-alkaline orogenic suite (Fig. 4c-e). On the other hand, the same diagrams for the biotite composition of Khunjerab pluton fall in between Fe-Mg-rich biotite of primary and calc-alkaline orogenic origin (Fig. 4c-e).

The chemical composition of the analysed plagioclase and K-feldspar of both areas (i.e., in samples KB1, KB10, KB13, KP1, and KP5) represents (or fall within) the potassium end-member of the alkali feldspar series (e.g., orthoclase-sanidine) and the members of the sodium-calcium plagioclase (e.g., oligoclase, andesine and labradorite; Supplementary Data Table S1A and B) on the ternary diagram shown in Fig. 5.

4.3. Whole-rock geochemistry and the principal component analysis (PCA)

Table 1 shows the results of the major and trace element compositions in a selection of samples (three from Khunjerab pluton and nine from Kohistan batholith). The results show a wide range of SiO_2 i.e., 67.5–73.3 wt.% and 60–71.4 wt.% for the Kohistan batholith and the Khunjerab pluton respectively. Principal component analysis has been used to create clusters of the samples based on geochemical parameters (Figs. 6-8). These clusters are shown with respect to various principal components (PCs). One of the plotted clusters i.e., the PC1 versus PC2 (Fig. 6 which represents ~ 74% of the data) show positively correlated variables; e.g., Na_2O and tungsten (W), that have been grouped together. On the other hand, variables that show negative correlations with SiO_2 are located in the opposite quadrants across the plot origin; e.g., Fe_2O_3 and REEs etc. Interpretation of the principal components is based on finding which variables are most strongly correlated with each component i.e., the degree of influence of variables on the factor map is proportionate to their distance from the plot origin. Which number (correlation value) is consider to be large or small is of course a subjective decision in a study. In this study, the PC1 and PC2 are considered to be strongly correlated with all the elements having a value equal or greater than 0.7. For example, PC2 has better representation of K_2O, Rb, U, and Th than PC1, yet both PCs have insufficient representation of Al_2O_3 and Sr. The high proportion of the major oxides and trace elements except those having correlation value less than 0.7, e.g., Al_2O_3, K_2O, U, Th, etc. indicates that PC1 most likely corresponds with the presence of compatible or incompatible materials. The combined plotting of both magmatic units is justified by the substantial similarities in the main rocks and mineralogy that they share, despite the differences in their geological settings and localities. The fractionation or crystallization pattern is seen in this plot by comparing the principal element oxides with SiO_2. For instance, SiO_2 exhibits weakly negative correlations with Al_2O_3 (13.28–16.22 wt.%; R^2 = 0.34), K_2O (1.12–5.35 wt.%; R^2 = 0.17), and Cr_2O_3 (0.002–0.007 wt.%; R^2 = 0.55). On the other hand, SiO_2 and Fe_2O_3 (1.15–5.61 wt.%; R^2 = 0.86), MgO (0.29–2.91 wt.%; R^2 = 0.92), CaO (1.52–5.58 wt.%; R^2 = 0.97), TiO_2 (0.07–0.73 wt.%; R^2 = 0.95), MnO (0.01–0.11 wt.%; R^2 = 0.76) and P_2O_5 (0.02–0.23 wt.%; R^2 = 0.85) exhibit higher negative relationships while Na_2O (2.44–5.24 wt.%; R^2 = 0.78) and SiO_2 have a strong positive correlation. The W (8.9–60.7 ppm) concentrations show weak/modest positive relationships with SiO_2, while Rb (14.1–172 ppm), Sr (119.4–748.9 ppm), Th (0.3–28.8 ppm), U (0.2–5.6 ppm), V (10–119 ppm), Ba (289–1305 ppm), and Ga (10.1–20.4 ppm) concentrations demonstrate weak negative correlation with SiO_2. On the other hand, Zr, Y, and all the remaining REEs shows strong negative correlation with SiO_2 (Table 1; Fig. 6).

To investigate the effect of pressure the clusters depicted on PC2 and PC3 is investigated, as illustrated in Fig. 7. In accordance to Alférez et al. (2022) and Chiaradia (2015), if PC3 give information about pressure, Sr exhibits a positive correlation with PC3, whereas Y exhibits a negative correlation. Between these two extremes the remaining REEs are distributed. However, elements with large ionic radii (K_2O and Rb) are positive, while elements with small ionic radii (i.e., MgO, Co, V, and Mn etc.) lie in the negative domain of the PC2 correlation graph (Fig. 7). The strong correlation amongst the Lu, Tm, Yb, Er, Y, Ho, Dy, and Tb is also existed in this plot (Fig. 7).

Clusters on PC4 and PC5 plot are analyzed to explore the influence of water (Fig. 8; Chiaradia, 2015; Alférez et al., 2022). Both the fluid-mobile Na_2O, K_2O, Sr, Ba, and Cs, and the immobile elements W, Co, and Sc show comparatively strong correlation with PC4. In

Table 1
Whole rock geochemistry from the Kohistan batholith (KB) and the Khunjerab pluton (KP) samples. N subscript represent normalized to the DM, while the T_{Zrsat} represent the zircon saturation temperature estimated using the methodology of Boehnke et al. (2013).

Sample No	KB1	KB2	KB3	KB7	KB8	KB10	KB11	KB13	KB14	KP1	KP4	KP5
Major oxides in weight percent (wt.%)												
SiO_2	67.54	73.36	69.58	69.19	70.68	70.20	69.07	67.53	73.34	59.97	71.47	61.60
Al_2O_3	15.73	15.00	15.88	15.94	13.28	13.72	15.92	15.55	13.92	16.22	13.67	16.11
Fe_2O_3	2.72	1.15	2.64	2.63	4.56	4.21	2.98	5.04	1.43	5.61	2.29	5.30
MgO	1.64	0.29	0.74	0.74	1.44	1.59	0.76	1.66	0.27	2.91	0.83	2.69
CaO	4.02	2.77	3.34	3.50	4.30	4.26	3.09	4.25	1.52	5.58	2.24	5.04
Na_2O	4.21	5.24	4.43	4.48	2.97	3.35	4.59	2.44	3.16	2.84	2.79	2.51
K_2O	1.66	1.12	2.15	2.03	1.40	1.37	2.15	1.81	5.35	2.62	4.57	3.69
TiO_2	0.29	0.07	0.32	0.32	0.31	0.31	0.34	0.45	0.13	0.73	0.24	0.68
P_2O_5	0.08	0.02	0.10	0.09	0.04	0.05	0.10	0.17	0.03	0.25	0.07	0.23
MnO	0.04	0.01	0.04	0.04	0.09	0.09	0.06	0.11	0.02	0.09	0.04	0.08
Cr_2O_3	0.006	0.002	0.002	0.002	0.002	0.002	0.002	0.002	0.002	0.007	0.002	0.007
Total	97.94	99.03	99.22	98.96	99.07	99.15	99.06	99.01	99.17	96.83	98.21	97.93
Trace element in part per million (ppm)												
Ba	561	488	607	598	388	463	302	289	721	1305	578	808
Ni	23	<20	<20	<20	<20	<20	<20	<20	<20	<20	<20	<20
Sc	6	<1	4	4	15	14	6	11	2	16	5	15
LOI (%)	1.9	0.8	0.6	0.9	0.8	0.7	0.8	0.8	0.7	2.8	1.6	1.8
Sum (%)	99.86	99.90	99.90	99.89	99.92	99.93	99.91	99.85	99.93	99.79	99.90	99.82
Be	<1	<1	1	1	<1	<1	<1	2	<1	2	<1	1
Co	10.6	3.6	6.3	6.1	13.2	12.4	5.8	11.9	7.0	13.8	8.5	12.0
Cs	0.40	0.20	2.00	2.00	1.00	1.00	2.40	3.60	1.00	1.60	1.60	2.00
Ga	13.5	14.8	17.3	17.8	10.1	10.6	20.4	16.9	16.6	18.8	13.5	19.2
Hf	2.0	1.7	2.5	2.6	2.6	2.4	2.9	7.1	3.1	5.6	3.5	5.1
Nb	1.3	1.3	2.8	2.9	1.0	1.3	7.1	6.9	3.1	12.2	9.4	11.9
Rb	32.5	14.1	67.8	64.6	33.7	38.8	78.3	87.9	104.8	95.4	172	123.2
Sn	<1	<1	<1	<1	<1	<1	2	1	<1	2	2	3
Sr	573.7	748.9	438.4	460.6	119.4	136.4	345.7	299.6	291.1	688.4	292.0	500.5
Ta	<0.1	0.2	0.3	0.2	<0.1	<0.1	<0.1	0.6	0.2	0.8	1.3	0.9
Th	2.5	2.3	8.5	8.9	0.3	0.4	11.5	8.0	15.3	13.0	28.8	15.2
U	0.3	1.1	3.0	3.0	0.2	0.3	2.0	1.6	2.1	2.1	5.6	3.0
V	73	15	45	47	95	85	39	48	10	119	35	113
W	30.0	19.0	23.5	22.2	26.2	15.2	16.5	8.9	60.7	23.6	59.0	20.6
Zr	76.6	49.7	93.5	96.4	84.8	76.7	107.5	331.4	95.4	219.5	117.1	196.2
Y	3.4	2.5	4.1	3.9	16.6	17.7	4.5	49.3	3.3	23.0	15.5	22.7
La	15.3	6.8	18.4	20.1	4.0	3.8	20.9	30.9	15.3	36.6	35.6	38.3
Ce	25.9	12.7	32.9	34.3	9.4	9.2	36.8	61.5	28.3	72.3	61.9	72.0
Pr	2.64	1.43	3.33	3.60	1.18	1.26	3.78	6.67	2.93	8.10	6.18	8.19
Nd	9.4	5.7	11.8	12.3	5.6	6.2	13.9	24.2	10.0	31.6	20.0	30.6
Sm	1.17	0.96	1.74	1.82	1.49	1.57	2.38	4.54	2.07	5.92	3.50	5.71
Eu	0.38	0.22	0.46	0.49	0.40	0.43	0.48	1.27	0.40	1.34	0.66	1.24
Gd	0.97	0.74	1.31	1.23	2.06	2.08	1.74	4.60	1.31	4.98	2.75	4.78
Tb	0.12	0.08	0.16	0.15	0.37	0.40	0.21	0.91	0.14	0.73	0.42	0.67
Dy	0.61	0.40	0.84	0.87	2.50	2.63	0.96	6.95	0.73	4.12	2.52	3.88
Ho	0.11	0.06	0.14	0.14	0.59	0.60	0.14	1.76	0.08	0.81	0.49	0.75
Er	0.35	0.19	0.39	0.43	1.82	1.85	0.35	5.67	0.28	2.38	1.46	2.28
Tm	0.03	0.03	0.05	0.04	0.29	0.30	0.03	0.86	0.04	0.32	0.23	0.32
Yb	0.30	0.20	0.33	0.34	2.00	2.12	0.27	5.45	0.22	2.24	1.66	2.16
Lu	0.04	0.03	0.04	0.04	0.32	0.34	0.03	0.87	0.03	0.33	0.25	0.31
Eu/Eu^*	1.09	0.80	0.93	1.00	0.70	0.73	0.72	0.85	0.74	0.75	0.65	0.72
$(La/Yb)_N$	34.71	23.14	37.95	40.23	1.36	1.22	52.68	3.86	47.33	11.12	14.60	12.07
$(La/Sm)_N$	8.19	4.44	6.63	6.92	1.68	1.52	5.50	4.26	4.63	3.87	6.37	4.20
$(Ce/Yb)_N$	22.73	16.72	26.25	26.56	1.24	1.14	35.88	2.97	33.87	8.50	9.82	8.78
$(Ce/Sm)_N$	5.37	3.21	4.58	4.57	1.53	1.42	3.75	3.28	3.31	2.96	4.29	3.06
$(Eu/Yb)_N$	3.63	3.15	3.99	4.13	0.57	0.58	5.09	0.67	5.21	1.71	1.14	1.64
T_{Zrsat} (°C)	650.3	628.7	675.4	675.7	660	648.9	689.3	824	686.3	715.8	702.3	711.4

addition, PC4 cluster include elements carried by hydrothermal transformation (like Co, Sc, Ga, and W), radioactive elements (including K and Rb), and the zirconium-hafnium combination (Alférez et al., 2022 and references there-in). This plot (Fig. 8) also shows that all the data are centred around the origin of the plot, suggesting no clear correlation between the degree of fractionation and water effects. The implication of Figs. 6–8 to the geology of the both the Kohistan batholith and Khunjerab pluton is detailed later in the discussion section.

4.4. Geochemical characterization

The major oxides in the samples of the Kohistan batholith and Khunjerab pluton were also investigated for the geochemical characterization and geochemical affinity as shown in Fig. 9. Oxides of the Kohistan batholith are located in the granodiorite and granite fields while that of Khunjerab pluton falls in the diorite, granodiorite, and granite region on the $Na_2O + K_2O$ versus SiO_2 diagram (Fig. 9a; Middlemost, 1994). The representative samples KB1,

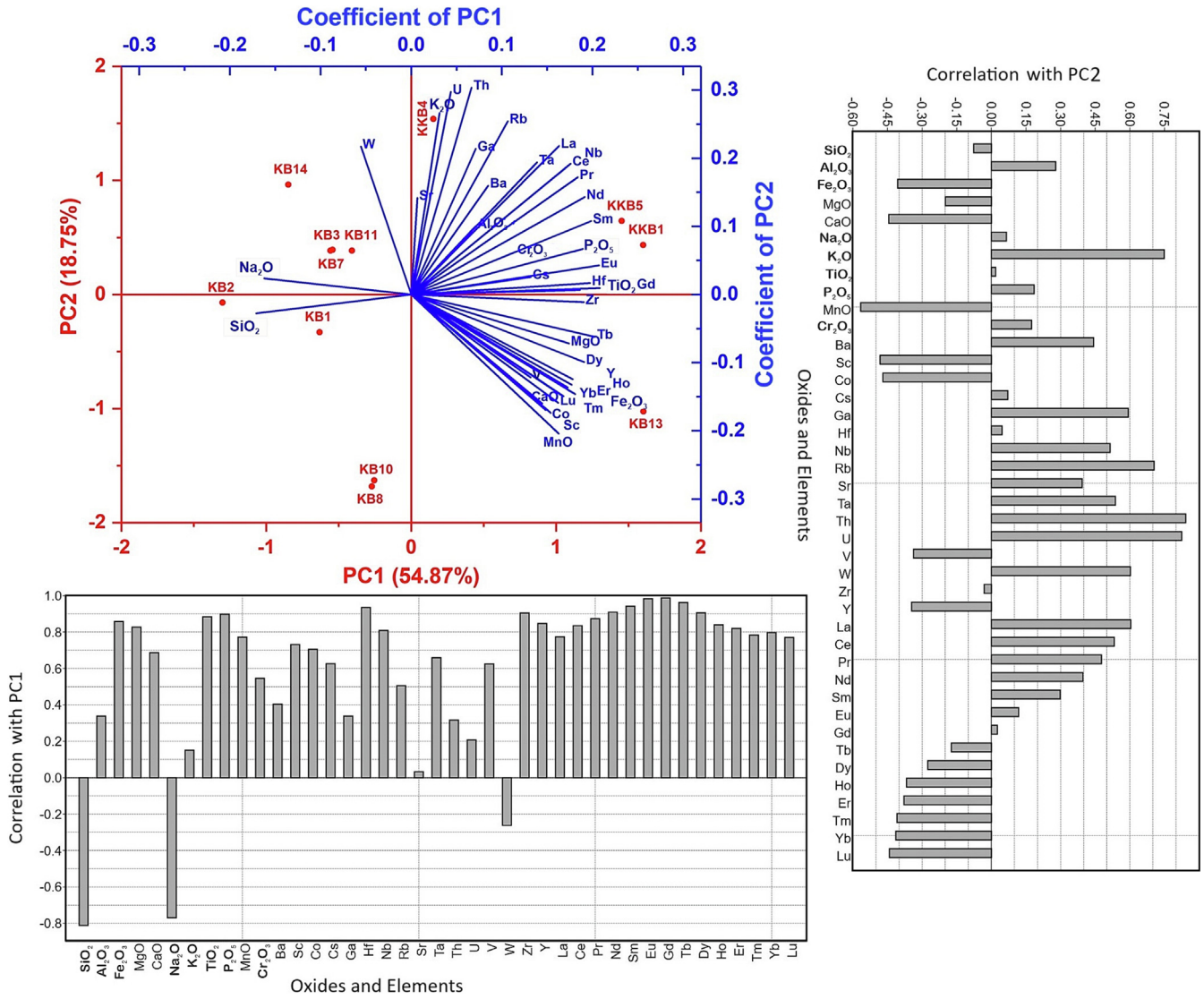

Fig.6. PCA vectors PC1 versus PC2 plot showing the cluster for the whole rock geochemical analysis. PC1 represents ~ 55% of the total data while the PC2 represents ~ 19% data. The bar plot adjacent to either axis of the plot shows the correlation of each oxide and trace element with PC1 and PC2.

KB10, KB13 of the Kohistan batholith falls in granodiorite, granite, and granodiorite respectively while the representative samples KP1, KP4, and KP5 lies in the region of diorite and granodiorite. All samples are magnesian according to the Fe-index diagram (Fig. 9b; Frost et al., 2001). On the SiO_2 versus (Na_2O + K_2O)-CaO plot, the samples from the Kohistan batholith indicate calcic to calc-alkaline composition and those of the Khunjerab pluton exhibit a calc-alkaline composition (Fig. 9c). All the samples of both magmatic units on a SiO_2 versus ASI plot (Frost et al., 2001) lie in the region of peraluminous to metaluminous granitoids (Fig. 9d).

Fig. 10 shows spider diagrams normalized against primitive mantle for the Kohistan batholith and Khunjerab pluton samples. The granites are characterized by enriched large-ion lithophile elements (LILEs) such as Rb, K, and U, and depleted high-field strength elements (HFSE) such as Nb, Zr, and Ti (Fig. 10a; Sun and McDonough, 1989) and also a notable depletion of Ba and P. Samples show an enrichment of the LREE compared to the HREE with moderate to high $(La/Sm)_N$ ratios ranging from 1.52 to 8.2 (N indicates normalization to chondrite values) for Kohistan batholith and 3.9–6.4 for the Khunjerab pluton samples. Further, both the Kohistan batholith and Khunjerab pluton samples exhibit negative Eu anomalies (Eu/Eu^* = 0.7–1.09) and (Eu/Eu^* = 0.65–0.75) respectively (Fig. 10b; McDonough and Sun, 1995).

On the AFM plot (Irvine and Baragar, 1971), all the data points lie in the calc-alkaline series (Supplementary Data Fig. S1a). Also, on the tectonic discrimination diagrams of Pearce et al. (1984), all the samples are located in the VAG and the *syn*-COLG fields (Supplementary Data Fig. S1 b-c). According to Whalen et al. (1987), most of the granitoids fall in the unfractionated granite field (OTG; Supplementary Data Fig. S2a, b). This suggests that the granitoids have an affinity to the classical I- and S-types, as is also shown by the Zr versus Ga/Al diagrams (Supplementary Data Fig. S2c). But the negative correlation of SiO_2 with P_2O_5 in all the samples more likely suggests an I- type granite affinity (Fig. 12d; Chappell, 1999). On plots of La versus La/Sm and Zr versus Zr/Nb (Allegre and Minster, 1978) , the samples of both the Kohistan batholith and that of the Khunjerab pluton show the formation of these granitoids dominantly via partial melting (Supplementary Data Fig. S2e, f).

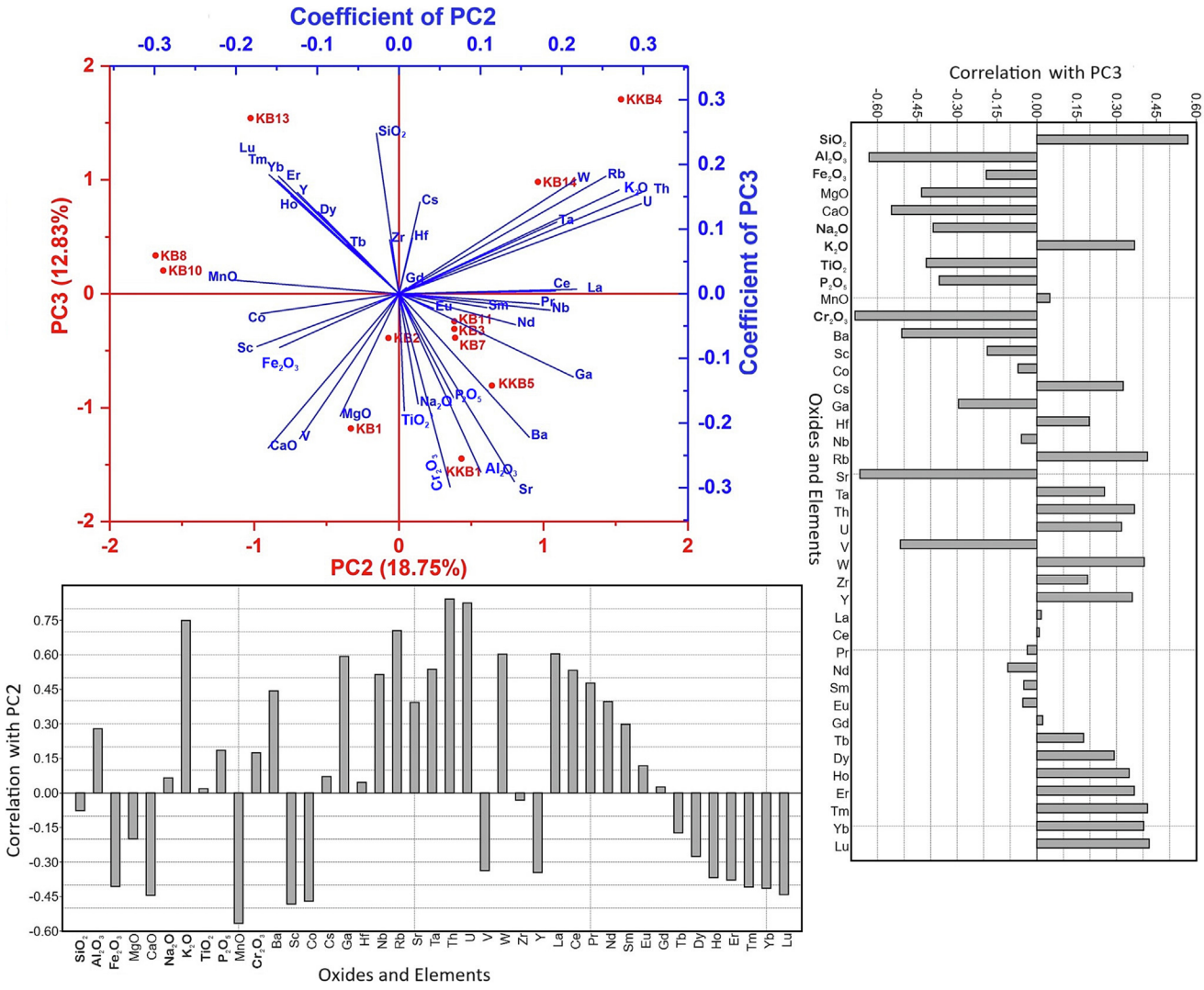

Fig.7. PCA vectors PC2 versus PC3 plot showing the cluster for the whole rock geochemical analysis. PC2 represents ~ 19% of the total data while the PC3 represents ~ 13% data. The bar plot adjacent to either axis of the plot shows the correlation of each oxide and trace element with PC2 and PC3.

4.5. Zircon U–Pb geochronology

The outcomes of the U-Pb analyses of zircons in samples KB1, KP1, and KP4 are presented in Supplementary Data Table S4 and are depicted on concordia diagrams (Figs. 11a–d, 12a–d and 13a–d). Each sample have zircon grains of different sizes and, on the cathodoluminescence (CL) images, primarily show moderate to strong oscillatory zoning. Their textures range from euhedral to subhedral (Figs. 11e, 12e, and 13e).

For sample KB1 which is a granodiorite, seventy spot analyses on 48 zircon grains show Th and U concentrations ranging from 60 ppm to 2680 ppm and 150 ppm to 1330 ppm respectively. Their Th/U ratios are in between 0.4 and 2.02 with an average of 0.61, suggesting a magmatic origin (Belousova et al., 2002). The zircons of Kohistan batholith show $^{207}Pb/^{235}U$ and $^{206}Pb/^{238}U$ apparent ages ranging from 89–150 Ma and 87–100 Ma, respectively (Fig. 11f) and giving a weighted mean age of 91.6 ± 0.27 Ma and 91.7 ± 0.28 Ma with MSWD values of 1.36 and 1.40, respectively. Here, it is the obtained crystallization age of the Kohistan batholith which falls in the late Cretaceous period (Fig. 11a-b). In Fig. 11c, the bars represent the apparent $^{206}Pb/^{238}U$ ages, while the shaded black line denotes the mean line with 95% confidence level (2σ). Accepted (concordant) data points are marked as magenta bars, discordant ones as green, and excluded ones as cyan colour. Fig. 11d displays a histogram of the same ages with magenta (accepted or concordant), green (discordant), and cyan (excluded) boxes. Additionally, kernel-density estimations for all data (dashed red) and accepted data (solid red) are included in Fig. 11d.

Zircon from sample KP1 which is a diorite in composition shows euhedral to subhedral grains under cathodoluminescence (CL); some grains show oscillatory or patchy zoning, while a minority of the crystals show no zoning at all (see Fig. 12a-f). Their Th/U ratios range from 0.57 to 1.21. Thirty-seven zircons from KP1 have been analyzed for $^{206}Pb/^{238}U$ and $^{207}Pb/^{235}U$ apparent ages, showing concordance at the 95% confidence level (2σ). These apparent ages range from 99 Ma to 116 Ma and 100 Ma to 141 Ma respectively. The weighted average $^{207}Pb/^{235}U$ age obtained from zircon of KP1 is 106.3 ± 0.4 Ma (MSWD = 1.79; see Fig. 12a), while the weighted average $^{206}Pb/^{238}U$ age of these zircon is 106.4 ± 0.4 Ma (MSWD = 2.0; see Fig. 12b). Fig. 12c–d show the bar plot and the weighted mean $^{206}Pb/^{238}U$ ages (solid black line) with the magenta colour bars denoting the accepted points, green the discordant, and the cyan colour representing the excluded points.

The zircon in samples KB1 and KP1 can be separated into two morphological groups: First group include the euhedral to subhedral crystals and crystal fragments with altered cores having weak

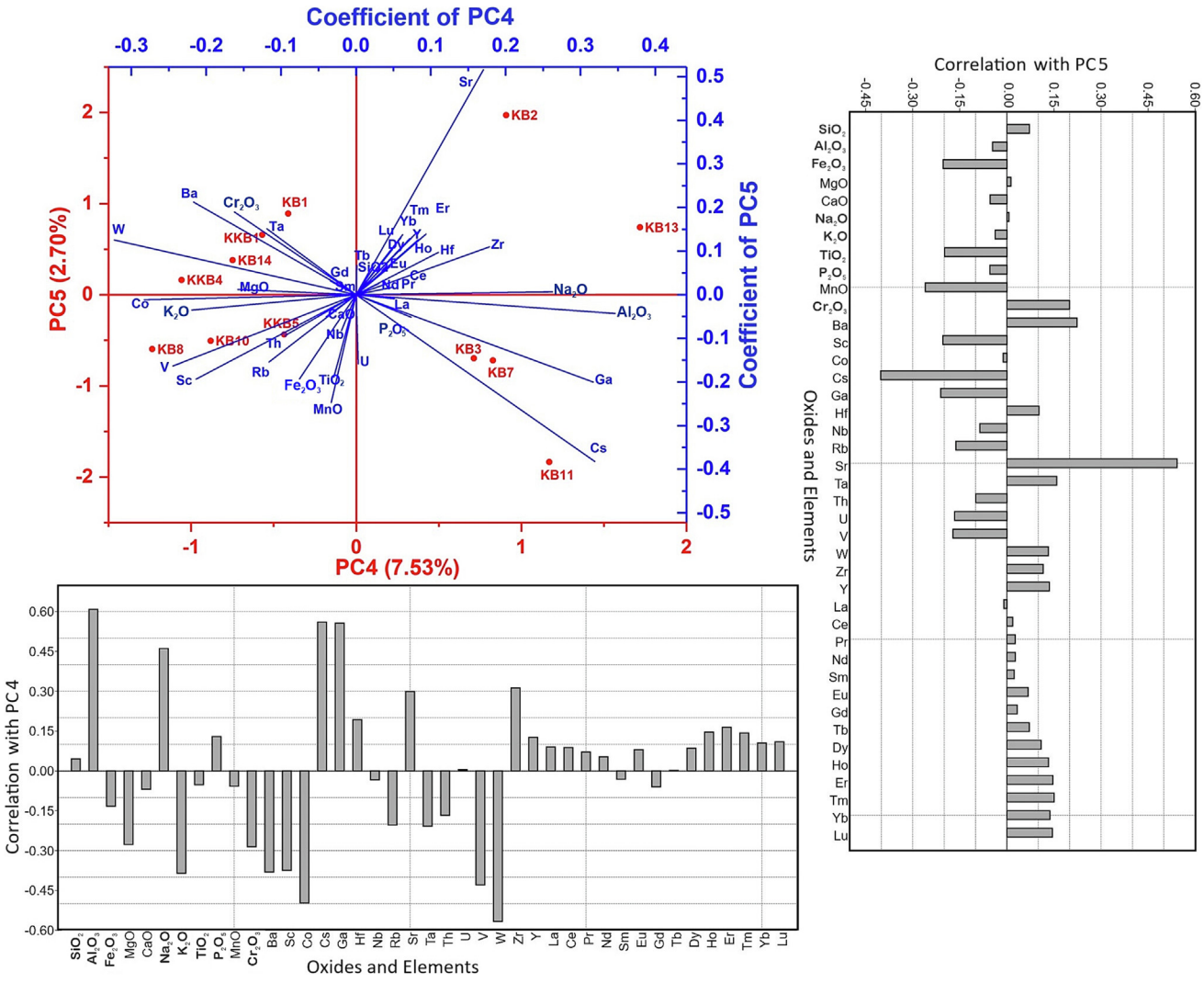

Fig.8. PCA vectors PC4 versus PC5 plot showing the cluster for the whole rock geochemical analysis. PC4 represents 7.5% of the total data while the PC5 represents 2.7% data. The bar plot adjacent to either axis of the plot shows the correlation of each oxide and trace element with PC4 and PC5.

to moderate oscillatory zonation (5% zircon grains in KB1 and 20%–25% grains in KP1; Supplementary Data Figs. S3, S4). Euhedral to subhedral crystals with nearly unaltered cores are included in the second group (95% zircon grains in KB1 sample and 75%–80% grain in KP1) that exhibits well established concentric oscillatory zoning (Supplementary Data Figs. S3, D4).

The zircon grains extracted from KP4 sample (which is also a diorite in composition) of the Khunjerab pluton display oscillatory or patchy zoning on CL images and are euhedral grains (Fig. 13a-f). The zircons exhibit Th/U ratios ranging from 0.6 to 0.86. Only four zircons have been analyzed from this sample showing $^{206}Pb/^{238}U$ and $^{207}Pb/^{235}U$ apparent ages ranging from 104.3 – 107.2 Ma and 104.7 – 111.8 Ma respectively. Together, these data yield a $^{206}Pb/^{238}U$ weighted average age of 106.44 ± 1.04 Ma (MSWD = 2.71; Fig. 13b) and $^{207}Pb/^{235}U$ weighted average age of 105.97 ± 1.03 Ma (MSWD = 1.94; Fig. 13a). Further, the Fig. 13c-d reflect the weighted mean $^{206}Pb/^{238}U$ ages with the magenta colour bars (accepted points), green colour bars (the discordant points), and the cyan colour bars (the excluded points).

4.6. Nano scale investigation of zircon using TEM analysis

Due to the chemical stability of zircon and its predisposition towards the limited incorporation/substitution of common Pb during crystal growth, zircon is a vital geochronological tool for U-Pb petrochronology. However, there are still some factors e.g., fluid-mediated alteration or metamictization, and chemistry that can significantly impact their age systematics (Villa and Hanchar, 2017). Further, distinct crystal domains show features related to the different concentration of REE that result in the formation of microscale to nanoscale heterogeneities in zircon crystals, and in diffusion–reaction processes in the metamict zones of the zircon (Vonlanthen et al., 2012; Tramm et al., 2021). The inclusions are in the form of zircon growths that are rich in Zr as compared to the ground mass zircon (Fig. 14; Vonlanthen et al., 2012; Tramm et al., 2021). Therefore, nanoscale investigations are vital and necessary to investigate the effect of nanoscale alterations on the U-Pb and other geochronometers.

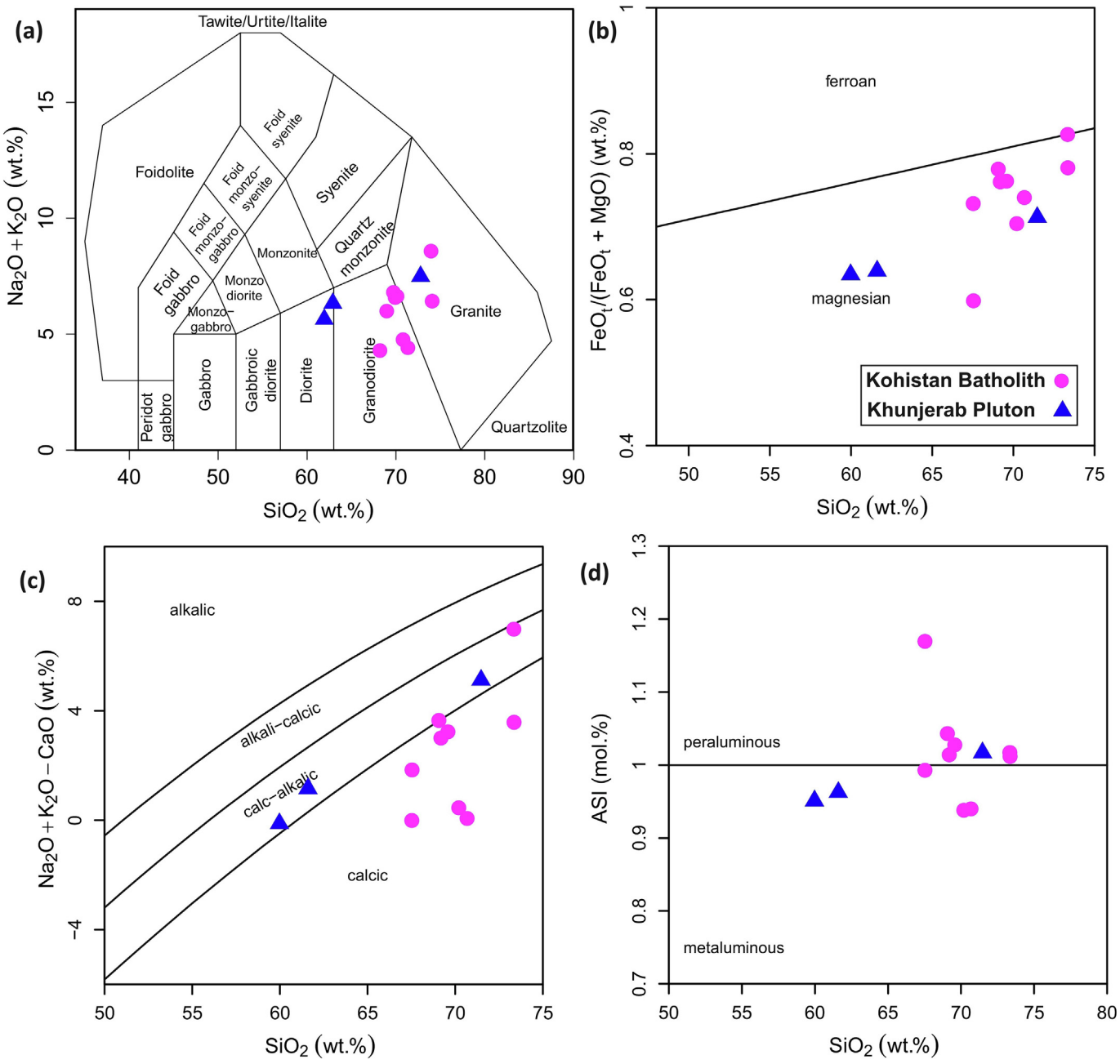

Fig.9. Classification diagrams for the geochemical affinity of the Kohistan batholith and the Khunjerab pluton using the classification (a) of Middlemost (1994), (b-d) of Frost et al. (2001).

Two TEM foils were prepared, one from the zircons of each intrusive body sample (KB1 is a granodiorite, and KP1 is a diorite). In HAADF mode, the zircon foil (46 – 61 nm thick; Fig. 14a) from the Kohistan batholith (sample KB1) shows a dark ground mass containing bright spots (Fig. 14b). In these bright spots, the EDX spectra indicate elevated Zr concentrations (~ 39 wt.%; Supplementary Data Table S5A) as compared to that in the slightly darker ground mass (~ 35 wt.%; Supplementary Data Table S5A; Fig. 14c-g). The bright spots may probably represent the later stage growth or the new nano-crystals of zircon. It is also observed that with increase in the Zr content the stability of the crystal increases as it forms ridges when the foil is bombard with same energy Ga ions during FIB milling (Fig. 14c–g). The inclusions (bright crystals) in the dark domain have higher Zr and therefore may probably have less REE or other elements that replaces Zr in the formula. Dark patches indicate loss/distort crystal integrity to significant level and decreases material density, which results in decreased electron scattering, whereas bright patches show stronger electron scattering and brighter contrast. Bright Field (BF) imaging reveals this variation in crystal integrity with reversed contrast, in comparison to HAADF. Brighter cloudy areas in the BF mode denote lower material density and crystallinity (Supplementary Data Figs. S5-S8). Furthermore, zircon diffraction patterns in HAADF show diffuse diffraction rings, indicating a metamict state (Fig. 14h) and that all because of the dominancy of the darker regions as compared to the brighter one. However, because of their small size (only a few nanometers) and interference with the surrounding zircon (in the background), their unambiguous identification is still

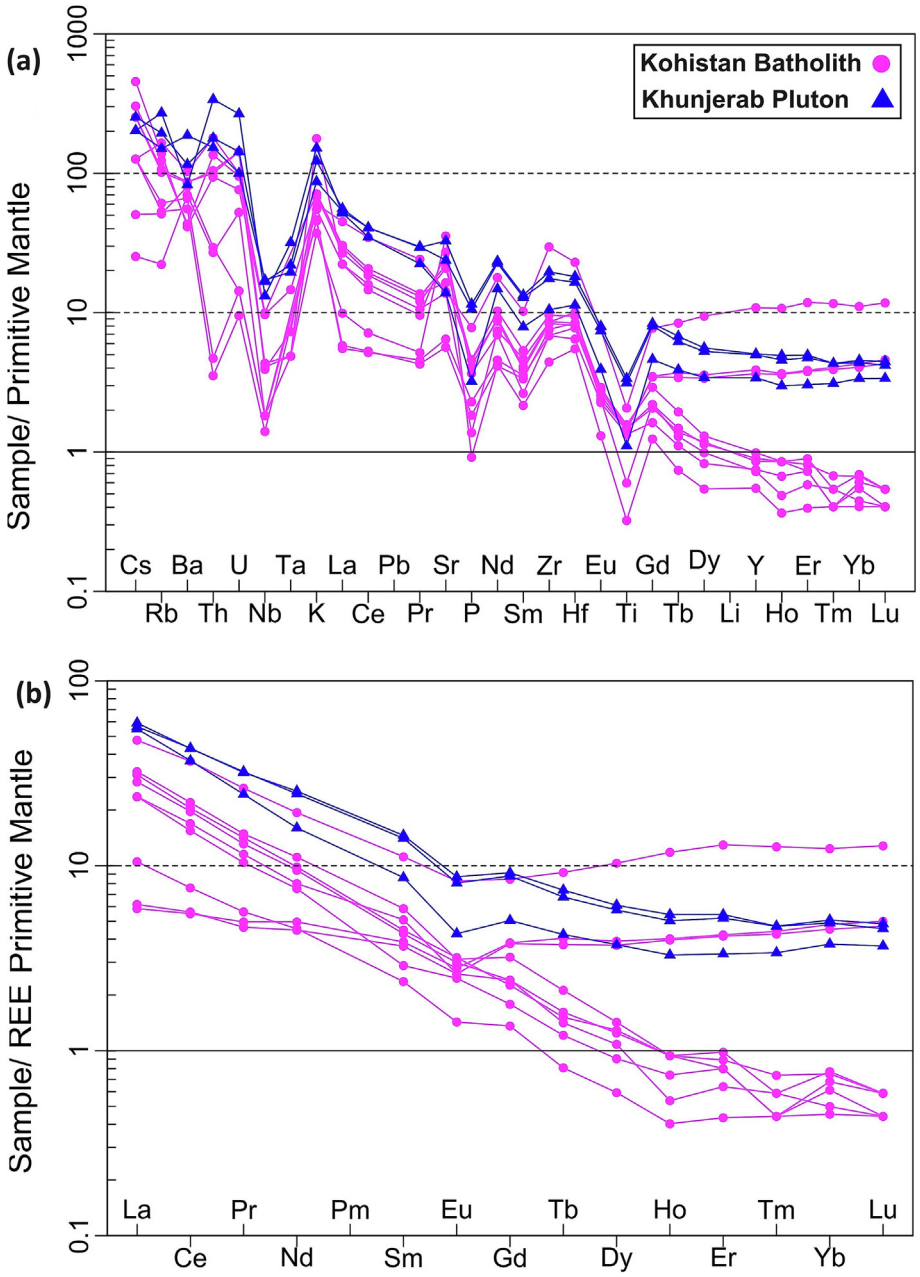

Fig.10. Display of the trace element and ree spider diagrams. (a) The trace element spider diagram normalized against primitive mantle using the method of Sun and McDonough (1989) and (b) REE primitive mantle-normalized spider diagrams using the methodology of McDonough and Sun (1995).

challenging. Certain zircon inclusions have a dark area surrounding them, which symbolizes the inclusions' or ridges' transmitted electron shadows as shown in Fig. 14e.

In HAADF mode the zircon foil from khunjerab samples (the diorite; Fig. 14i) having thickness ranging from 43.7 nm to 52.5 nm, the dark and bright patched display irregular or wave-like patterns (Fig. 14j–o). The bright patchy domains (Zr = ~43 wt.%; Supplementary Data Table S5B) and dark patchy domains (Zr = ~40 wt.%; Supplementary Data Table S5B; Fig. 14j–o) at the nanoscale represent variable Zr concentration indicating the incorporation of different REEs and hence different state of metamictization as compared to the investigated zircon from the Kohistan batholith (Fig. 14p). This illustrates how varying degrees of crystallinity can be produced by even small changes in the REE contents. However, there is no evidence of the nano scale inclusions in the representative zircon foil from the Khunjerab samples and the REEs are typically distributed irregularly within the sample (Fig. 14j–o). Some nano-veins in the foil of zircon from khunjerab pluton are also observed (Fig. 14k) filled with relatively dark texture which may indicate slightly high accumulation of REEs in this zone. The size of these nano-veins is only few nanometers and the proper elemental detection cannot be made with the EDX attached to the TEM. In HAADF mode of zircon foil from KP1, the diffraction patterns show diffuse diffraction rings relatively more intense than that of KB1, indicating more metamictization in the zircon samples of Khunjerab pluton (Fig. 14p).

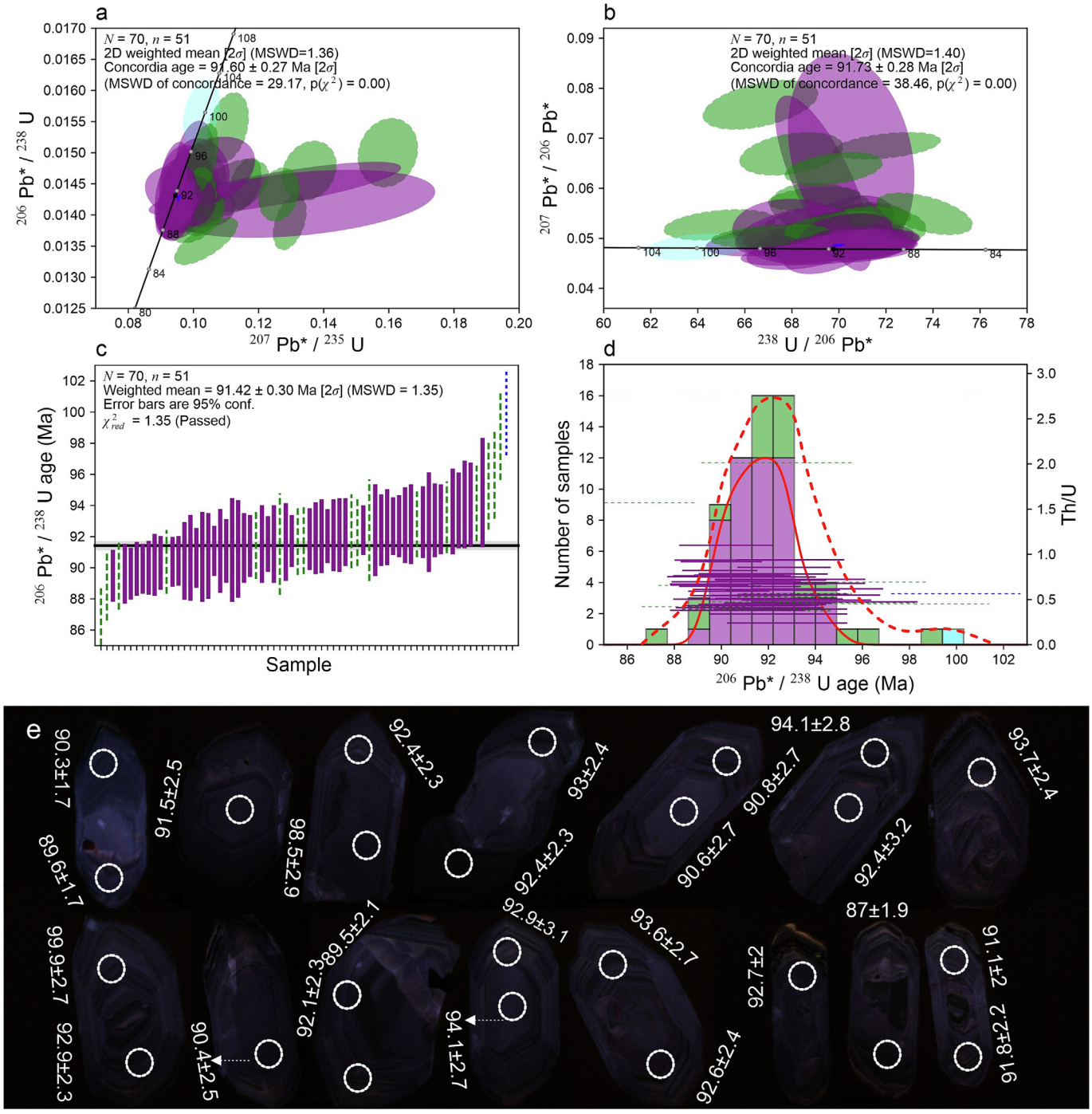

Fig.11. (a) Conventional Wetherill concordia plot along with the error ellipses of 95% confidence level. Here, the magenta colour denotes the accepted points, green the discordant, and the cyan colour represent the excluded points. A blue ellipse on the concordia curve represents the concordia age for the sample KB-01 of the Kohistan batholith. The symbols N and n stand for accepted measurements and total measurements, respectively. (b) Tera-Wasserburg concordia diagram having the same legends as that for diagram (a). (c) A bar plot showing the weighted mean (black line) with 95% confidence level prepared for the $^{206}Pb^*/^{238}U$ ages. Measurements that are accepted, discordant, and the excluded one are represented by magenta, green and cyan colour bars respectively, (d) $^{206}Pb^*/^{238}U$ age histogram having same legend as (a). Additionally, the estimated kernel densities for all points (denoted by dashed red line) and the accepted points (solid red line) are also shown here. The y-axis on the right side of the plot shows the Th/U ratios with same symbol as in (c). (e) The zircon with labelled spots and their corresponding U-Pb ages.

5. Discussion

5.1. Petrogenesis of the Kohistan batholith granitoids

Mineral fractional crystallization plays a major role in the evolutionary process of magmatic rocks. For instance, granitic rocks rich in silica can be formed through the fractional crystallization of mafic magmas (Shellnutt, 2018; Bohrson et al., 2020; Heinonen et al., 2020). These types of magma on the other hand may result from partial melting of hydrated basaltic or gabbroic rocks in the oceanic crust (Bohrson et al., 2020; Heinonen et al., 2020). Experimental results show that basaltic compositions that melt due to dehydration processes produce silica-rich arc-like magmas (Ulmer, 2001). However, the initial water in the protolith

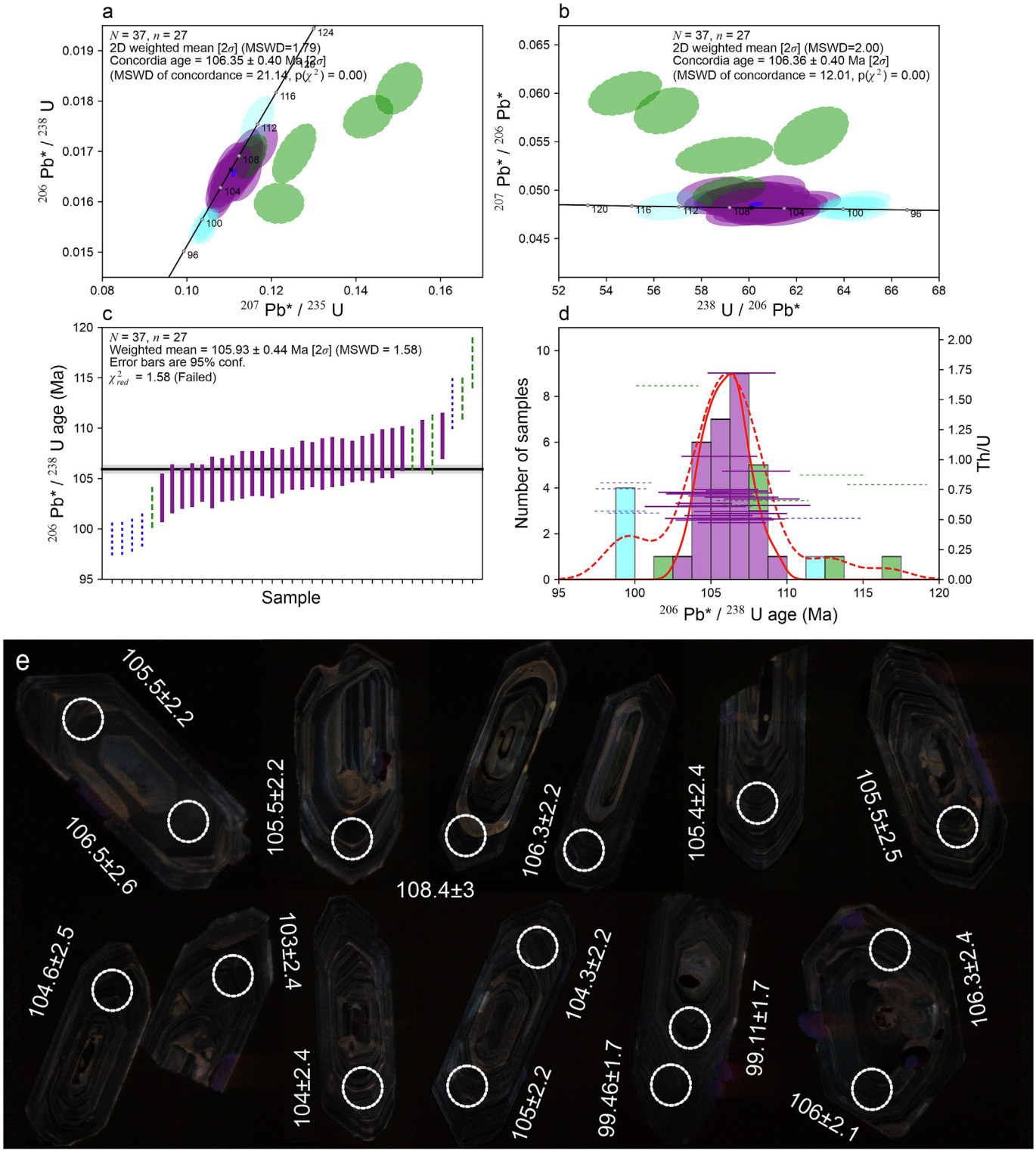

Fig.12. (a) Conventional Wetherill concordia plot along with the error ellipses of 95% confidence level. Here, the magenta colour denotes the accepted points, green the discordant, and the cyan colour represent the excluded points. A blue ellipse on the concordia curve represents the concordia age for the sample KP-01 of the Khunjerab pluton. The symbols N and n stand for accepted measurements and total measurements, respectively. (b) Tera-Wasserburg concordia diagram having the same legends as that for diagram (a). (c) A bar plot showing the weighted mean (black line) with 95% confidence level prepared for the $^{206}Pb^*/^{238}U$ ages. Measurements that are accepted, discordant, and the excluded one are represented by magenta, green and cyan colour bars respectively, (d) $^{206}Pb^*/^{238}U$ age histogram having same legend as (a). Additionally, the estimated kernel densities for all points (denoted by dashed red line) and the accepted points (solid red line) are also shown here. The y-axis on the right side of the plot shows the Th/U ratios with same symbol as in (c). (e) The zircon with labelled spots and their corresponding U-Pb ages.

may not surpass the water content of the hydrous mineral phases such as amphibole, biotite, and plagioclase. Based on the analyzed amphibole chemistry of the representative samples KB10 (granite) and KB13(granodiorite) in this work, the Kohistan batholith show estimated (using the methodology of Ridolfi, 2021 and references there-in) water contents of 8 – 10 wt.% at 2 – 4.3 kbar (Fig. 15a-

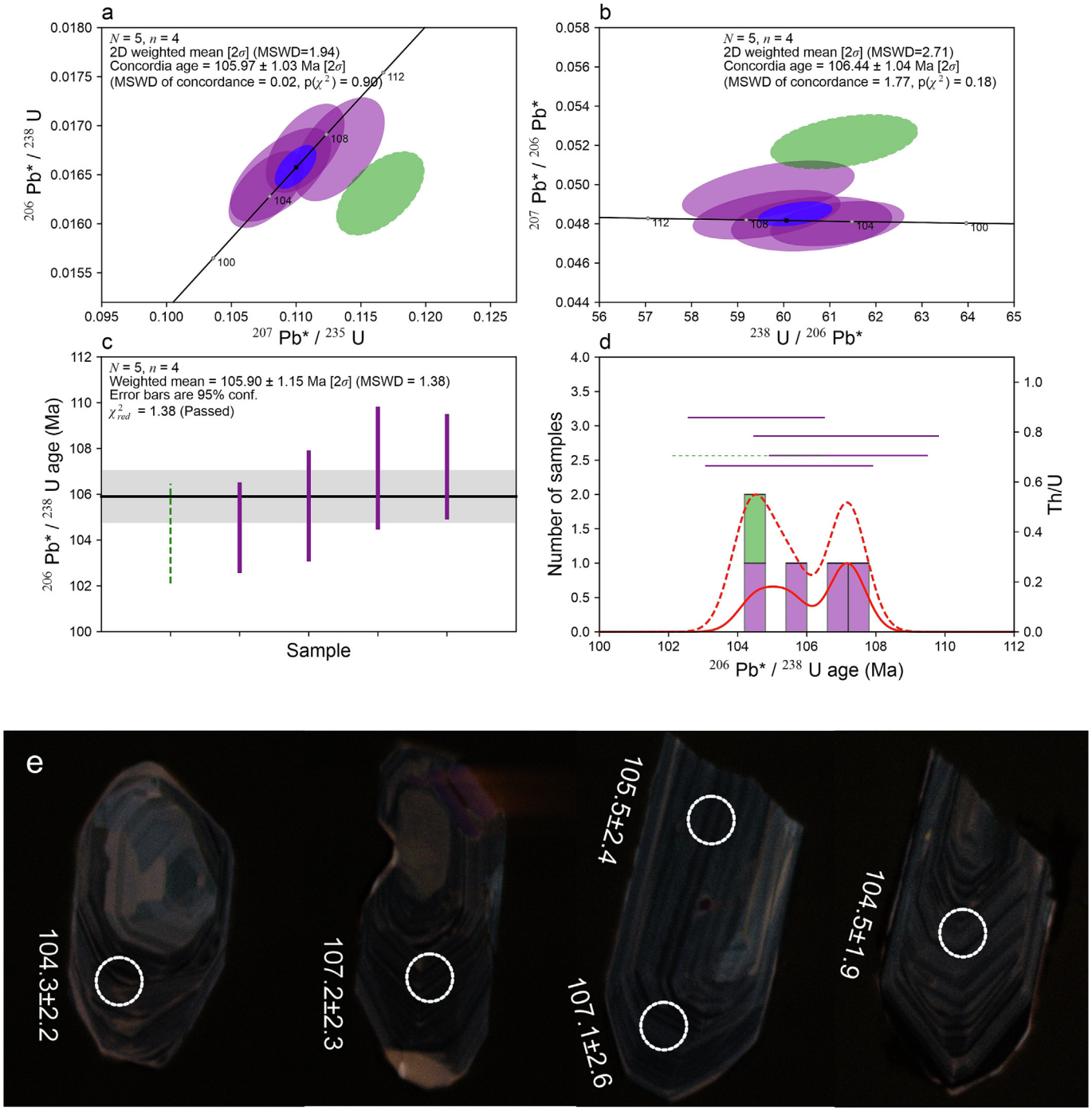

Fig.13. (a) Conventional Wetherill concordia plot along with the error ellipses of 95% confidence level. Here, the magenta colour denotes the accepted points, green the discordant, and the cyan colour represent the excluded points. A blue ellipse on the concordia curve represents the concordia age for the sample KP-04 of Khunjerab pluton. The symbols N and n stand for accepted measurements and total measurements, respectively. (b) Tera-Wasserburg concordia diagram having the same legends as that for diagram (a). (c) A bar plot showing the weighted mean (black line) with 95% confidence level prepared for the $^{206}Pb^*/^{238}U$ ages. Measurements that are accepted, discordant, and the excluded one are represented by magenta, green and cyan colour bars respectively, (d) $^{206}Pb^*/^{238}U$ age histogram having same legend as (a). Additionally, the estimated kernel densities for all points (denoted by dashed red line) and the accepted points (solid red line) are also shown here. The y-axis on the right side of the plot shows the Th/U ratios with same symbol as in (c). (e) The zircon with labelled spots and their corresponding U-Pb ages.

b). Amphibole typically crystallizes before plagioclase in water-rich magma during the fractionation process and slow magmatic differentiation (Bohrson et al., 2020). Therefore, the amphibole chemical analysis can reveal important details about petrogenesis, such as tectonic setting, geochemical traits, and crystallization conditions. The amphibole of the Kohistan batholith samples ranges from pargasite to clino-ferro-suenoite in composition (Fig. 3). This suggests that the pargasite is from magmatic origin while the clino-ferro-suenoite input represent some high pressure and temperature crystallization or incorporation from surrounding rock in close contact with the melt. The pargasite composition of the Kohistan batholith denotes the crystallization and/or re-

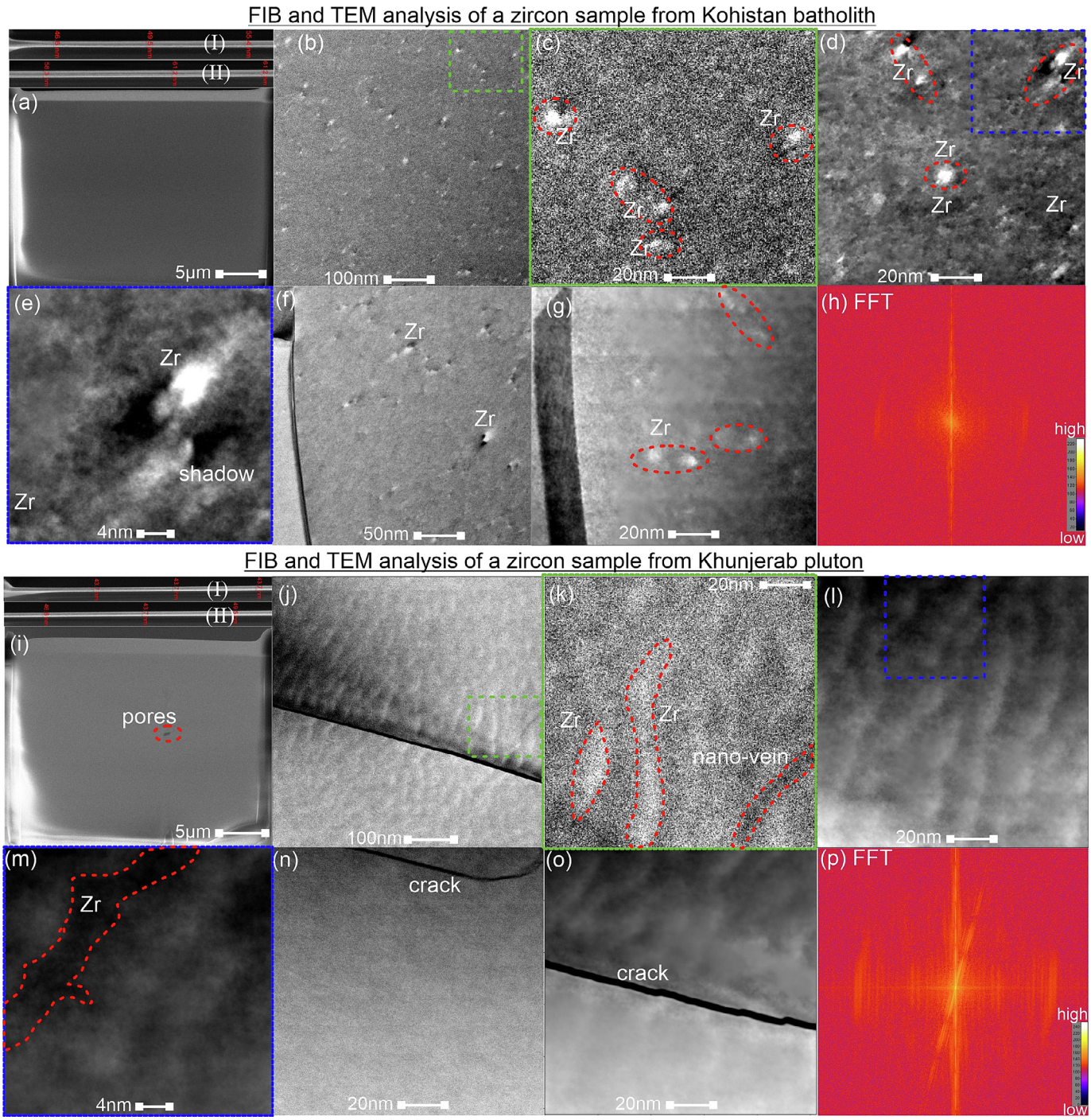

Fig.14. Zircon TEM microphotographs from the Kohistan batholith (a–h) and the Khunjerab pluton (i–p). (a) The foil overview, (b) shows two asymmetric zoning areas divided by rough and smooth surface features, (c) the zoom image of these rough crystal inclusions marking the same mineralogy with slightly high Zr concentrations, (d-f) the filtered and zoom image of these nano-crystals. The filter image is displayed after applying the Topaz-Denoise filter of Bepler et al. (2020). (h) Fast Fourier transform (FFT) based diffraction patterns clarify the structure of the slight uneven domains/metamictization in the zircon of Kohistan batholith. (i) The foil overview of the zircon from Khunjerab pluton, (j) shows two asymmetric zoning areas showing wavy dark and bright smooth surface bands like features, (k) the zoom image of these surfaces with nano-vein having the darker morphology, however, the bight band have slightly high Zr concentrations. (l–o) The filtered and zoom image of the foil. The filter image is displayed after applying the Topaz-Denoise filter of Bepler et al. (2020). (p) Fast Fourier transform (FFT) based diffraction patterns clarify the structure of the uneven and high metamict zircon (of Khunjerab pluton) than that of the Kohistan batholith.

equilibration at a low oxygen fugacity, at temperature range of 780–830 °C, and at moderate pressure of 2 kbar to 4.3 kbar based on EPMA-based geochemical analysis as shown in Fig. 15a–c.

Biotite in the representative samples of Kohistan batholith (KB1; granodiorite, KB10, and KB13) shows low to moderate levels of Fe^{2+} (i.e., $Fe^{2+}/(Fe^{2+} + Mg)$ = 34.8%–57.6%; Supplementary Data Table S2A). In essence, the oxygen fugacity and the total Fe content of the rock can both have an impact on biotite composition and stability in the ilmenite series. Rather than higher bulk rock Fe content, a decreased oxygen fugacity and temperature is thought to be the cause of the elevated Fe content in the biotite found (Fig. 16a, b). The Fe# of biotite (Supplementary Data Table S2A) varies signif-

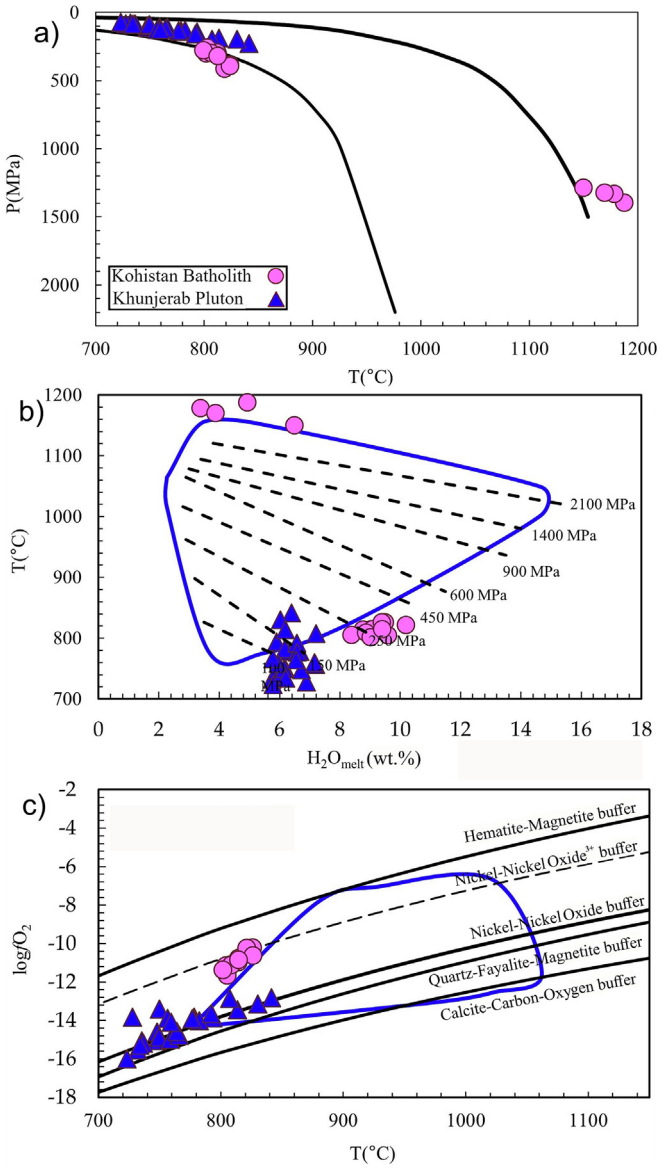

Fig.15. Plots showing the (a) *P* versus *T* plot, (b) a plot of *T* versus H_2O_{melt}, and (c) give the logfO_2 versus *T* diagrams estimated from the mineralogical composition of amphiboles of Kohistan batholith and Khunjerab pluton. Isobars are indicated by the dashed lines in (b), while the most typical metal–metal oxide buffers in (c) are inserted from Hirschmann et al. (2008).

icantly, indicating variable oxygen fugacity conditions (Fig. 16b). Thus, the compositions of calcic amphibole and biotite all point to a low oxygen fugacity during the crystallization of the rocks of the Kohistan batholith. Further, the petrographic and EPMA investigation of the representative samples (i.e., in KB1, KB10, and KB13) of Kohistan batholith also shows the predominance of K-Feldspar and plagioclase which falls in the composition of orthoclase-sanidine, and sodium-calcium plagioclase (e.g., oligoclase, andesine and labradorite; Fig. 5a).

In a discontinuous series, the amphibole (780–830 °C) tends to crystallize first, followed by biotite (above 500 °C and in the range 630–700 °C; Fig. 16; Henry et al., 2005). This is also indicated by the negative correlation of Dy and Yb with SiO_2 (Fig. 6; Smith, 2014) and their possible further depletion due to the growth of magmatic garnet (as indicated by the positive correlation of HREEs (Dy – Lu) with Y, SiO_2, Fe_2O_3, MnO, and CaO; Figs. 6 and 7; Hönig et al., 2014). Moreover, the negative correlation between SiO_2, CaO and Sr (Fig. 6) offer more proof of plagioclase fractionation (at 852 –1006 °C as estimated from EPMA data using Kudo and Weill, 1970). The inclusion of Th, Ce, and La in the structure of crystallizing silicate phase(s), like allanite, is strongly supported by the positive correlations that Th, Ce, and La have with silica and among themselves (Figs. 6 and 7; Hermann, 2002), and the allanite grains are present in the thin sections. The effect of hydrothermal alteration can be seen from the elements like Co, Sc, Cs, Ga, and W (Allegre and Minster, 1978; Alférez et al., 2022), radioactive elements (including K and Rb), and the Zr-Hf combination (Fig. 8). Fig. 8 also indicates that the effect of hydrothermal fluids is considerable as PC4 versus PC5 plot represents 10% of the total data.

All of the Kohistan batholith samples show calcic (mostly) to calc-alkaline (slightly), peraluminous to metaluminous, and magnesian characteristics (Fig. 9). Normalized to the primitive mantle, the data show enrichment in LREE and LILE such as Cs, Rb, U, and K compared to Ta and Nb (Fig. 10a), while depletion in Nb, Ta, Ti and Ba, a pattern resembling those of the Late Jurassic to Early Cretaceous granitoids in the west central Lhasa terrane, Tibet (Cao et al., 2016). When compared to the HREE [$(Tb/Yb)_N$ = 0.74 – 2.82] of the Kohistan batholith REE data, the REE plots (Supplementary Data Fig. S1) show an enrichment in LREE [$(La/Sm)_N$ = 1.52 – 8.2], indicating that the parent melt most likely came from a source rich or enriched in LREE. In the Kohistan batholith some samples show Eu anomalies and some show Ho and Tm anomalies indicating the crystallization of plagioclase and garnet (Fig. 10b). The tectonic discrimination diagrams suggest a VAG origin in an active compressive orogenic setting and unfractionated I- and S-type granite (i.e., Fe # > 0.6 (0.62 to 0.84), ASI = 0.9 to 1.2 (Fig. 9d), Zr/Hf = 29.2 to 46.7, Th/U = 1.3 to 8.3, and Nb/Ta = 6.5 to 15.5; Figs. 11a-c and 12a-f) indicating subduction related tectonic setting during the late Cretaceous at 91.7 ± 0.3 Ma (Fig. 11). Supplementary Data Fig. S2d shows that all rocks clearly show a trend of decreasing P_2O_5 as SiO_2 increases, which is an important indicator for differentiating between S-type and I-type granites. According to Wolf and London (1994), this is due to apatite tending to dissolve more easily in strongly peraluminous melts while it reaches saturation (A/CNK < 1.1) in metaluminous and slightly peraluminous magmas. Furthermore, a pattern that is consistent across all samples indicates that Th increases with increasing Rb levels (as both lies in the positive quadrants of the plot as shown in Fig. 6). This pattern is consistent with the typical evolutionary trends found in I-type granitoids, as reported by Chappell (1999), Cao et al. (2016), and Ali et al., (2024). However, according to Gao et al. (2016), it is not feasible to categorize granites merely based on the relationships between A/CNK and SiO_2, P_2O_5 and SiO_2 or Na_2O, K_2O, CaO and trace element concentration, e.g., Zr, Ce, Nb, Y, and Ga, because different magmatic processes, such as partial melting (dominated the formation of most granitoids of Kohistan batholith; Supplementary Data Fig. S2e-f) and fractional crystallization significantly influence the compositional differences (major and trace elements) among granites. Therefore, these lithochemical correlations may lead to ambiguous conclusions about the origin of granites.

Two main mechanisms are generally recognized for the formation of intermediate to felsic I-type magmatism in arc-related subduction zones. Firstly, the original magma experiences fractional crystallization within the crust (Grove et al., 1997, 2003; Wu et al., 2016). Secondly, a hybrid magma that is a mixture of lower crust and hot mantle wedge-derived hydrous basaltic magma which is partially melted. Integrating the data with that of Petterson and Windley (1991), the Kohistan batholith samples of this study show similarity with portions of stage 1 and stage 2 plutonic rocks that show the typical calc-alkaline chemistry associated with subduction processes. The magma of the Kohistan batholith has low initial $^{87}Sr/^{86}Sr$ ratios (ca. 0.7042; Petterson

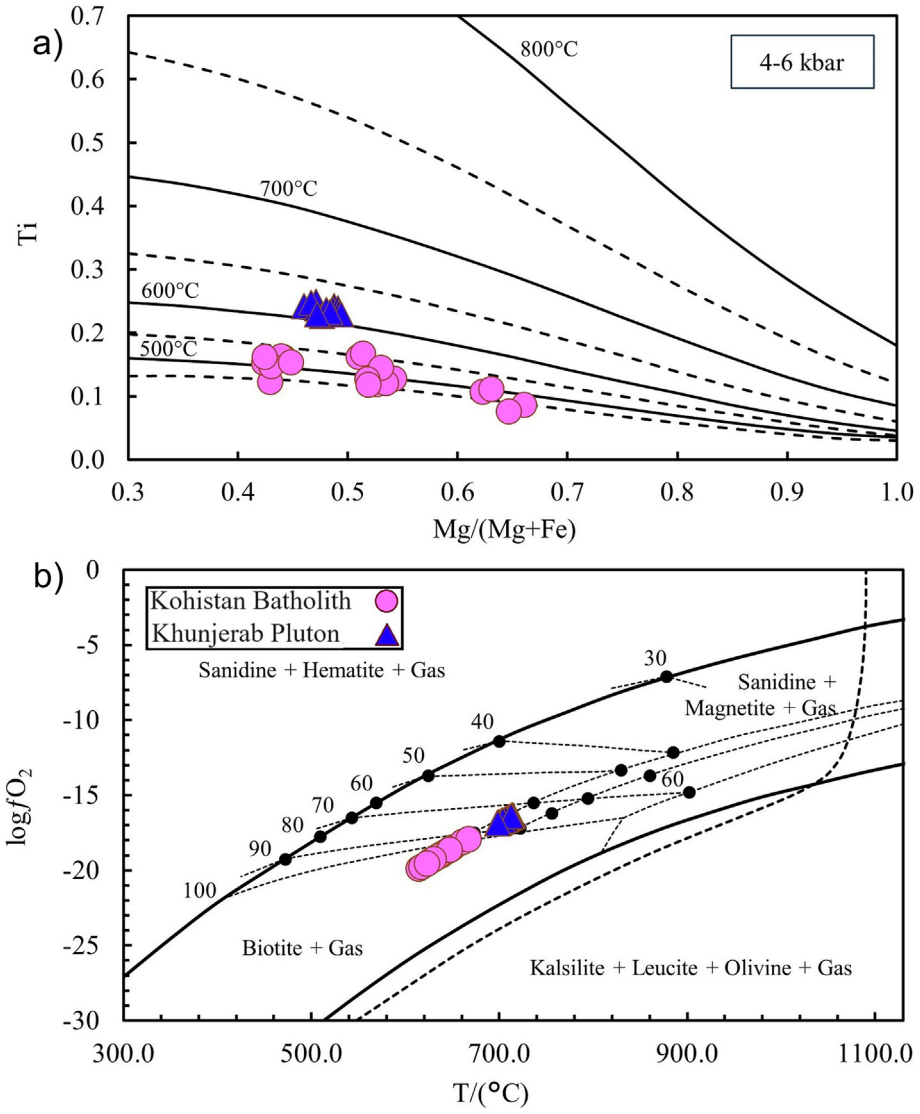

Fig.16. Variations diagrams of Ti against Mg/(Mg + Fe) ratio in the biotite composition extracted from the Kohistan and Khunjerab granitoids (diagram after Henry et al., 2005) and (b) show the logfO_2 versus T diagrams estimated from the mineralogical composition of the same biotites. The dashed line shows the probability in percent of the biotite + gas buffer (Wones, 1989).

and Windley, 1991; Argles et al., 2003), as well as enrichments in LILE compared to HFSE (i.e., Nb, Ta, and Ti) and LREE compared to HREE respectively (Fig. 10a). A metasomatized mantle wedge, fluid/melt addition from the subducting plate, subduction-related fluid enrichment, and an active compressive orogenic setting are all indicated by the high ratios of La/Nb = 3 to 12, Sr/Nd = 12 to 131, Ba/Nb = 42 to 432, and trace element plots respectively (estimated from Table 1; Supplementary Data Fig. S1; Chilson-Parks et al., 2022). Further, the Kohistan batholith has hydrous minerals (i.e., amphibole and chlorite) and high-water content as estimated from the mineral chemistry in the representative samples of this study indicates fluid activities in mantle wedge. Therefore, the source material of the magmas is believed to be a typical mantle that underwent metasomatism due to subduction-related processes. A more likely scenario is that different levels of subduction-related metasomatism occurred at the source, with high-K magmas coming from more altered regions and low-K magmas coming from less altered magma sources. As a result, the magma source is understood to be a mantle wedge above an active subduction zone that experienced variable metasomatism.

5.2. Petrogenesis of the Khunjerab pluton granitoids

The compositions of the amphiboles in the investigated samples of the Khunjerab pluton fall within the range of tremolite to pargasite and having a water content of 5.8 –7.0 wt.% at pressure of 1–2 kbar (Fig. 15a-b), suggesting partial melting and fractional crystallization of these amphibole at shallower depths than the Kohistan batholith. The pargasite composition of the Khunjerab pluton samples shows the crystallization and/or re-equilibration in the presence of low oxygen fugacity and temperature range of 720–850 °C (Fig. 15). Fig. 5 show the composition of biotite in Khunjerab pluton sample which fall within the Fe-Mg rich composition, re-equilibrated, and of a calc-alkaline orogenic suite. It has moderate levels of Fe^{2+} (Fe# = 51%–54%; Supplementary Data Table S2B) and water content range from 3.2–3.4 wt.%. The Fe^{+2} content of the biotite does not show much variation indicating low oxygen fugacity (Fig. 16b). Therefore, the approximately balanced Fe and Mg content of the biotite is due to lower oxygen fugacity and higher temperature. These analysis shows that the amphibole (720–850 °C) crystallizes first followed by the

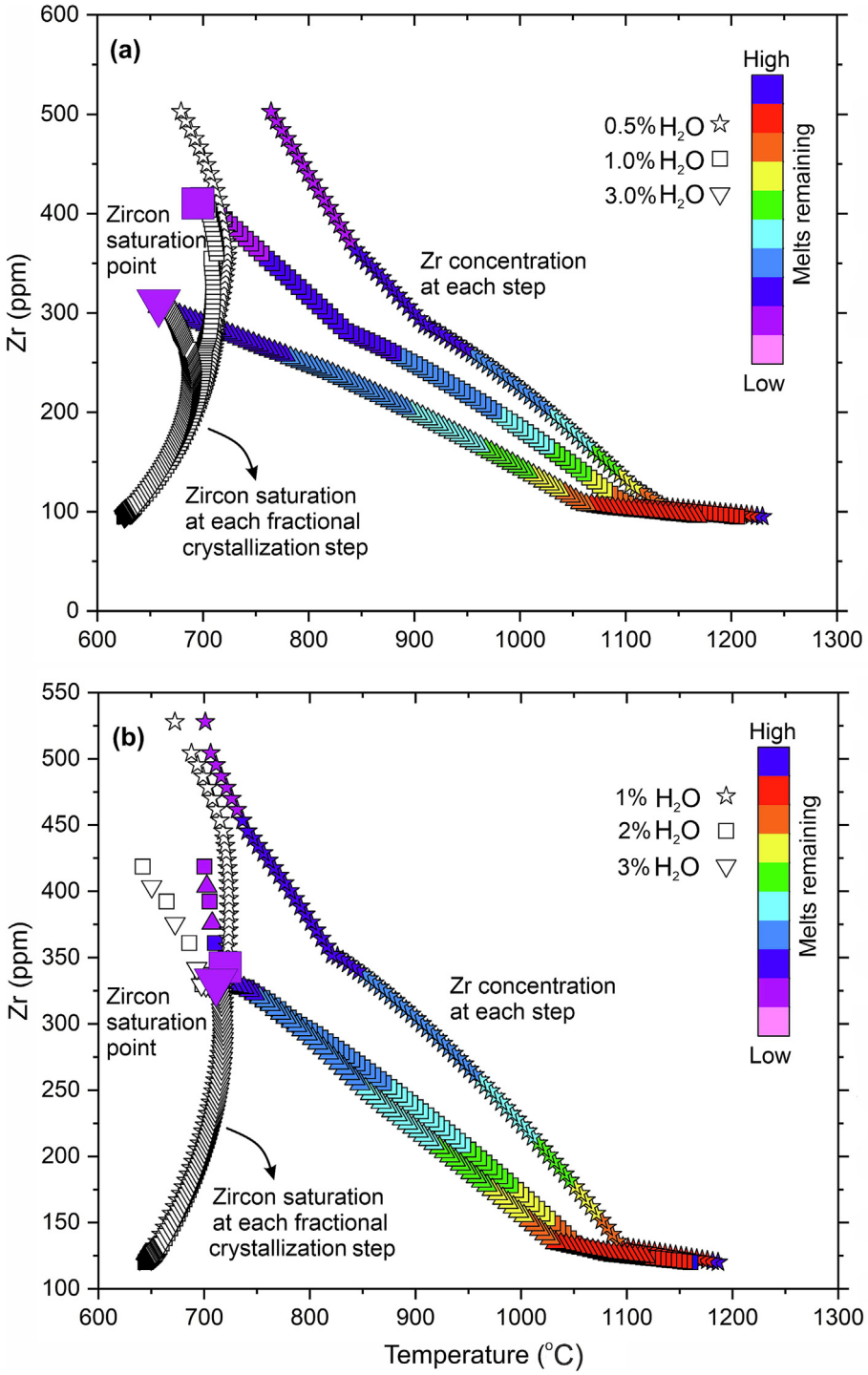

Fig.17. Modeled Zr and zircon saturation evolution in the samples of (a) the Kohistan batholith and (b) the Khunjerab pluton. Together with the variation in zircon saturation temperature versus Zr concentration at each fractional crystallization step, the plot also displays the modeled Zr concentration against the melt temperature and fraction of the melt remaining. Zircon will saturate in the melt at the point where the Zr concentration curve coincide with the zircon saturation temperature; this point is indicated by a big magenta rectangle and triangle.

crystallization of biotite (> 600 °C to 700 °C; Fig. 16). The plagioclase on the other hand crystallized at 987–1115 °C according to the thermo-barometric equation of Kudo and Weill (1970).

Normalized to the primitive mantle, the trace elements of whole rock samples from the Khunjerab granites show enrichment in Rb, U, and Th compared to Ta and Nb (Fig. 10a), a pattern resembling the few samples from Kohistan batholith (Fig. 10a) and that in Crawford and Searle (1992). The granite's REE patterns match the traits of I-type granites. When compared to HREE [$(Tb/Yb)_N$ = 1.13–1.45], their REE show an enrichment in LREE [$(La/Sm)_N$ = 3.9–6.4], indicating that the parent melt most likely came from a source rich or enriched in LREE. One characteristic shared by all the three samples of the Khunjerab pluton is the presence of a negative Eu anomaly, which points to the early crystallization of plagioclase.

The plot of the whole rock geochemical data presented in this study using the tectonic discrimination diagram of Whalen et al.

(1987) suggests a VAG origin of the Khunjerab samples in an active compressive orogenic setting (Supplementary Data Figs. S1, S2) and it suggests, that the samples can be classified as I-type granite because $FeO_t/(FeO_t + MgO)$ ratio is greater than 0.6 range from 0.66 to 0.73, Zr/Hf range from 33.5 to 39.2, Nb/Ta from 7.2 to 15.2, and Th/U range from 5.06 to 6.19 (Table 1). However, the most distinctive feature is that P_2O_5 shows a strong negative correlation trend with SiO_2 which is the typical characteristic of an I-type granite (Chappell, 1999; Cao et al., 2016; Gao et al., 2016). Moreover, Th increases with increasing Rb in the Khunjerab pluton, which is consistent with the general evolutionary trend of I-type granite.

The geochemical data of the Mid-Late Cretaceous intermediate-felsic intrusive bodies to the north of the main Karakoram batholith (Crawford and Searle, 1992; Debon and Ali Khan, 1996; Ogasawara et al., 1992, 2008; Reichardt et al., 2010) also shows the nature of calc-alkaline I-type granitoids. Their analyses also show that these magmatic bodies have low to moderate ($Na_2O + K_2O$)/CaO ratios, variable A/CNK ratios, lower HFSE concentrations and noticeable negative Eu anomalies (Crawford and Searle, 1992; Fig. 10a). Further, the photomicrograph and EPMA analysis of the Khunjerab samples show plagioclase (dominantly albite) with well observed twining (Fig. 2g and Fig. 5), amphibole, biotite, zircon, apatite, and garnet. Therefore, the Khunjerab pluton are classified as normal calc-alkaline I-type granitoids (Whalen et al., 1987; Chappell, 1999).

According to the plots of La–La/Sm and Zr–Zr/Nb (Supplementary Data Fig. S2e-f), the Khunjerab pluton samples are characterized by linear trend which implies that most granitoids are formed by partial melting. According to Cao et al. (2016), granitoids samples formed by partial melting show moderate type negative Eu anomalies implying that biotite, plagioclase, and K-feldspar have only slightly fractionated. It also indicates that primary derivation from partial melting was dominant. The apatite fractionation is implied by the significant decrease in P_2O_5 with increasing SiO_2 (Supplementary Data Fig. S2d), especially for the granites. To summarize, it can be inferred that the Khunjerab pluton magmas may probably be originated from the partial melting of a mafic lower crust with significant alteration in the source region.

The magma for the I-type granitoids of the Khunjerab pluton has low initial $^{87}Sr/^{86}Sr$ ratio (ca. 0.714) as reported in Crawford and Searle (1992) and is within the same range as reported by Hawkesworth et al. (1979) and Argles et al. (2003) in similar environment. It is also characterized by an enrichment in LILE compared to HFSE and LREE compared to HREE respectively (Fig. 10a) and have high ratios of La/Nb = 3 to 4, Sr/Nd = 15 to 22, Ba/Nb = 61 to 107 (Table 1 and Supplementary Data Fig. S1; Chilson-Parks et al., 2022) which shows indication of a metasomatized mantle wedge, having fluid/melt addition from the subducting plate, subduction-related fluid enrichments in an active compressive orogenic/subduction related tectonic setting. Further, the fluid activities in mantle wedge are also indicated by the presence of hydrous minerals (i.e., amphibole and chlorite) and estimated high-water content using the mineral chemistry in the representative samples (KP1 and KP5) of Khunjerab pluton. Therefore, it can be inferred that the magma source for the Khunjerab pluton is a mantle wedge that had experienced metasomatism.

In summary, the compositional patterns of the investigated samples from both units are not exactly similar, but in most cases lies in the same sections of the geochemical affinity and classification diagrams (Figs. 9–10). However, differences are noticeable in their petrography and chemistry (Fig. 2). Additionally, Table 1 shows that they have different zircon saturation temperatures (T_{Zrsat}). The calculated zircon saturation temperature values according to Boehnke et al. (2013) for the Kohistan batholith and Khunjerab pluton are 682 ± 56 °C (629–824 °C) and 710 °C± 6.9 °C (702–716 °C) respectively. Fig. 10 shows significant differences between the two in terms of the magnitude of the Eu and Tm anomalies, depletion in elements such as P, Ti, and HREE, and enrichment in elements such as Th, U, and LREE. In addition, compared to the Khunjerab pluton, the Kohistan magmatic samples exhibit lower average MgO, K_2O, Fe_2O_3, CaO, Ba, and Nb and higher average SiO_2.

5.3. Early to late Cretaceous pre-collisional magmatism in KLIA and Karakorum block

Previous ages for the igneous rocks of the Kohistan batholith show significant variation. The U-Pb zircon ages vary from 111.5 – 41 Ma (Heuberger et al., 2007; Khan et al., 2009) while the Rb-Sr (whole rock) ages show ranges from 102 – 41 Ma (Petterson and Windley, 1985; Heuberger et al., 2007; Khan et al., 2009). In the Kohistan-Ladakh region, recent U-Pb zircon isotopic analyses have revealed the ages of volcanic and plutonic rocks, which date back to about 154 million years ago (Schaltegger et al., 2002; Ali et al., 2024). Heuberger et al. (2007) reported that rocks in the western region of Kohistan including quartz-diorites, basaltic sills, and granite dikes have ages of ~ 107 Ma and ~ 112 Ma. Prior research has also revealed U-Pb ages for granites greater than 95 Ma (Schaltegger et al., 2002), and ~ 101 Ma in Ladakh (Schärer et al., 1984). The Teru Volcanic Formation and a diorite sample from the Kohistan region show a U-Pb zircon age of about 65 Ma which is significantly younger than the aforementioned arc ages (154 Ma to approximately 100 Ma; Schaltegger et al., 2002). Further, in the Kohistan-Ladakh block they have also reported the youngest known zircon age, which is roughly 61 Ma for a granite in Ladakh (Schärer et al., 1984). Khan et al. (2009) interpret these young ages as an indication of the end of igneous activity within the calc-alkaline volcanic island arc of the Kohistan-Ladakh region and propose that they indicate the beginning of arc collision with the Indian plate along the Indus suture (Fig. 1).

By contrast, some of the U-Pb zircon ages of about 41 Ma were also found in some plutons (e.g., Pingal pluton) located close to the northern edge of the Kohistan-Ladakh block within the Kohistan batholith (Heuberger et al., 2007; Khan et al., 2009). This result implies that the Karakoram-Kohistan Suture Zone's magmatic and tectonic processes continued into the Eocene. They also figure out the involvement of the continental basement materials in the intrusions within the Kohistan-Ladakh block based on isotopic evidence that helps determine the timing of the Shyok suturing event (collision or closure of the ocean that connects the Kohistan Island Arc to the Karakorum (Eurasian) margin) during this time (Krol et al., 1996) According to Heuberger et al. (2007) and Khan et al., (2009), tectonic activity continued in the Kohistan-Ladakh block even after the Shyok suturing process was completed, some 50 Myr ago.

To gain further insight into the geological history of this geologically complex zone, the evolution of magmatism on the Eurasian/Karakoram side is of equal importance (Fig. 1). The Karakoram Batholith is a major granitic body in the Karakoram block (southern margin of Asian Continent before KLIA collision) formed due to the northward subduction (ocean-continent) related magmatism (Early Cretaceous). Nonetheless, a series of minor granitic units/plutons referred to as the Khunjerab-Tirich Mir granite belt are situated to the north of the Karakoram Batholith. Ogasawara et al. (1992) studied different granitoids in this belt, specifically in the Khunjerab valley. According to Ogasawara et al. (2008), the zircon of the Khunjerab pluton shows a weighted mean age of 112 Ma (107–120 Ma) and K-Ar ages of 96.9 ± 4.8 Ma and 107 ± 5 Ma for biotite and hornblende respectively. This is not the same age range as the K-Ar biotite ages reported by Treloar et al. (1989), which put the Khunjerab granodiorite cooling age

at 107 ± 5 Ma and 105 ± 5 Ma. According to Ogasawara et al. (2008), the Khunjerab granodiorite U-Pb age indicates that at approximately 110 Ma ago continental arc magmatism was active along the Asian continent's southern border. Furthermore, the Tirich Mir granite (pluton) close to Khunjerab pluton shows a Rb-Sr whole rock age of 115 Ma (Desio, 1964) and an altered biotite, giving a two-point age of 103 ± 2 Ma (Villa et al., 2001), an age similar to the Khunjerab granodiorite of Ogasawara et al. (2008). This discussion suggests that regionally widespread Mid-Late Cretaceous continental arc magmatism occurred along the southern edge of the Asian continent.

Keeping this in mind further LA-ICPMS analyses were performed here which show more refined and detailed ages for this widespread magmatism in the KLIA and the Karakoram region. Summarizing the outcome of our U-Pb dating with published Early to late Cretaceous pre-collisional magmatism, the new zircon U–Pb data for intermediate to felsic intrusive (KB1; granodiorite) rocks from the Kohistan batholith show apparent ages ranging from 87 Ma to 100 Ma (Fig. 11f; Supplementary Data Table S4) with weighted mean age of 91.7 ± 0.3 Ma (Fig. 11b). This magmatic epoch most likely documents a major, widespread magmatic event composed of granite and diorite to granodiorite. On the other hand, the results of the zircon U-Pb ages obtained in this study from KP1 and KP4 (both are diorite in composition) samples of Khunjerab pluton (Karakorum part of the KLIA-Karakoram (Asia) collisions) shows a main magmatic stage with apparent ages range from 99–116 Ma and a weighted average age of 106.4 ± 0.4 Ma (Figs. 12-13) which is consistent with the results of Ogasawara et al. (2008) and references there-in). The age differences in the main magmatic period for the Kohistan batholith sub-terrane (KLIA terrane) and the Khunjerab pluton (part of Karakorum terrane) suggests a different geodynamic framework in these two regions. The data reveal the different nature of partly coeval magmatism in these units, i.e., continental arc magmatism in the Karakoram (106.4 Ma) and arc magmatism on the Kohistan side (91.7 Ma) which is in agreement with previous studies of Petterson and Windley (1991), Heuberger et al. (2007), Khan et al. (2009), and Ali et al. (2024).

5.4. Effect of nano scale heterogeneities on u-pb systematics of magmatic zircons

By analysing the analytical and geochemical uncertainties of the zircon grains provide a wide range of dates (Supplementary Data Table S4) due to chemical heterogeneity and metamictization (Fig. 14). Pb diffusion is strongly related to the accuracy and reliability of U-Pb dating for zircon and other geochronometers (Cherniak and Watson, 2001; Ullah et al., 2023a, 2023b). Variations in chemical composition, point defects, vacancies, dislocations, and radiation damage are some of the variables that influence the diffusion of radiogenic lead in minerals (Ullah et al., 2023a, 2023b and references therein). Fig. 14 shows the chemical heterogeneity and metamictization for the representative samples (i.e., KB1 and KP1) used in the dating of the rocks of Kohistan batholith and Khunjerab pluton. The bright spots in the zircons of Kohistan batholith (Fig. 14c-g; which probably represents the later stage growth or the new nano-crystals of zircon) indicates the stability of the crystal as it forms ridges when milled with the same energy Ga ions during FIB milling. Only these zones have lower concentrations of REEs (i.e., U, Th and other REEs) and other Zr formula replacement elements (i.e., Hf; Vonlanthen et al., 2012; Tramm et al., 2021).

According to studies by Djimbi et al. (2015) and Gautheron et al. (2020), blockage is crucial in preventing Pb mobility, especially in zircon. Trapping is another important feature that affects how Pb and other elements diffuse in minerals. Gautheron et al. (2020) andUllah et al. (2023a) have reported such trapping effect when vacancies (which are frequently created during irradiation) are created provide an area of lower energy to the diffusing Pb atom and as a result trapping takes place. The vacancies may either be due to displacing Zr, Si, or O atoms within the crystal lattice, Pb atoms in zircon may become stuck in the atomic vacancies that result in lowering its diffusion (because removing the Pb atom from the vacancy requires more energy (Ullah et al., 2023a)). As Kusiak et al. (2015) highlight, trapping may be experimentally demonstrated in the form of nanospheres/nanocrystals. In general trapping may results when a diffusing atom(s) find lower-energy regions inside the crystal lattice for accommodation.

One of the most efficient trapping mechanisms in zircon is radiation damages/metamictization, which results in vacancies and amorphized zones (Fig. 14c-e, k-m). Defects caused by radiation have a major impact on Pb diffusion because they frequently remain in zircon producing variety of microstructures (Fig. 14k, m). Zircon crystals do not completely anneal radiation-induced damage, even at temperatures higher than 1000 °C (Ewing et al., 2003). The incorporated younger zircon overgrowth crystals (Fig. 14c) and the microstructures (Fig. 14k, m) probably occupied by REEs have led to these mixed ages (87–100 Ma for KB1 and 99–116.7 Ma for KP1). Because, in HAADF imaging, bright patches with lower concentrations of U and Th typically preserve the crystal structure better than darker patches having higher concentrations of these elements (Vonlanthen et al., 2012; Tramm et al., 2021). The REEs occupied veins which may have formed due to the irradiation damages distort crystallinity and can be seen from the diffraction pattern in TEM images (Fig. 14h, p). It also shows that the Khunjerab pluton sample are more metamictized as compared to that of Kohistan batholith. It can also be seen in the inclusions (bright crystals) in the dark domain which have higher Zr and therefore may probably have less REE or element that replace Zr in the formula and are therefore less metamictized (Fig. 14). This illustrates how varying degrees of crystallinity can be produced by even small changes in the REE contents and may probably affect the U-Pb ages (Ullah et al., 2023b). Therefore, the variation in the U-Pb ages or the reasons of the discordance ages of zircons from Khunjerab pluton samples are more (despite a smaller number of dated zircon) as compared that of Kohistan batholith. This implies that the closure temperature and diffusion kinetics are significantly impacted by radiation damage, metamictization, and chemical heterogeneities (Fig. 14; Ullah et al., 2023a, 2023b). Consequently, differences in zircon ages may arise even when the zircons are collected from the same rock.

5.5. Thermal modelling of the magmatic events

To test zircon saturation and the influence of the initial water content of the metasomatized melt using hit and trail analysis with Magma chamber simulations (Bohrson et al., 2020; Heinonen et al., 2020), the chemical compositions of the sample close to that of Ali et al. (2024) was taken as a starting material for the Kohistan batholith magmatic chamber modelling. This sample probably reflects the initial melt composition of the Kohistan batholith samples while the sample KP1 is used as a representative or starting composition for the Khunjerab pluton. The modelling was done with an initial water content range from 0.5%–3% for the samples of both areas with an oxygen fugacity at the NNO buffer, pressures between 2 and 4 kbar for Kohistan batholith and 1–2 kbar for Khunjerab pluton (as inferred from mineral chemistry of amphibole Fig. 15), and temperatures between 700–1200 °C. The Zr concentration in the modelled samples was ~ 96 ppm (Kohistan batholith) and ~ 120 ppm (Khunjerab pluton). Zircon saturation conditions can be found by evaluating the melt's degree of polymerization, which is indicated by the cation ratio (Na + K + 2Ca)/

(Al × Si) and is represented as M (Boehnke et al., 2013). Lower degrees of polymerization and higher zircon solubility can be inferred from the higher M values. The zircon saturation temperature using the whole rock data is estimated to be in the range of 628–824 °C for KB samples and a range of 702–715 °C for samples from KP (Table 1).

By using the forward modelling techniques of rhyolite-MELTS (Gualda et al., 2012; Gualda and Ghiorso, 2015), it is possible to gain a better understanding of the zircon saturation conditions in these magmatic units. At the said pressure–temperature conditions and temperature-dependent partition coefficient of Zr with the mineral phases present at each fractionated stage of magma chamber, the Zr concentration in the melt and the zircon saturation temperature is estimated after each fractionated steps using the formulas presented by Boehnke et al. (2013). The likely point of zircon saturation is indicated where both the Zr concentration and saturation intersect (Fig. 17). The model in Fig. 17 shows how the water content affects zircon saturation conditions by varying the initial H_2O concentrations in the melt from 0.5 wt.% to 3.0 wt.%. It should be noted that the liquid composition from which zircon crystallizes is similar to that of a granite, containing roughly 70–73 wt.% SiO_2 for all the initial H_2O concentrations. This dependency results from H_2O's suppression of silicate saturation e.g., zircon saturation happens at about 700 °C after ~ 87% of the magma has been crystallized, with an initial H_2O concentration of 1.0 wt.%. On the other hand, increasing the initial H_2O concentration decreases the amount of fractional crystallization that is needed and lowers the temperature at which zircon saturation occurs. According to our modelling, zircon saturation is reached at about 650 °C after reaching ~ 80% fractional crystallization at an initial H_2O concentration of 2.0 wt.%. Similarly, for the sample of KP, the zircon saturation occurs at about 720 °C and 705 °C after ~ 90% and ~ 80% fractional crystallization with an initial H_2O concentration of 2.0 wt.% and 3.0 wt.% respectively.

Comparing the results of T_{Zrsat} estimated from the whole rock geochemical analysis of Table 1 and that obtained from the modelling suggest that apart from the Zr concentration and M values, H_2O also affects the Zr saturation temperature. It also shows that the closest match of the T_{Zrsat} value in comparison to Table 1 is achieved between 1%–2% and 2%–3% water in the melt for the Kohistan batholith and the Khunjerab pluton, respectively, which is comparable with Table 1 and the typically hydrous minerals (amphibole and biotite) identified in the samples of both the Kohistan batholith and the Khunjerab pluton (Supplementary Data Table S1 and S2). The higher initial water in the melt of the Khunjerab samples is also in agreement with the considerably larger amount of amphibole and biotite as compared to the Kohistan batholith. Thus, these models proposes that both area units have experienced fluid activity at the source regions of magma and reflect the crystallization from a magma source of metasomatized mantle wedge nature.

On the other hand, the thermal histories estimated for both magmatic units using samples KB1, KP1, and KP4 show normal cooling trajectories. The conventional model proposes a gradual cooling period that occurs at a rate of ca. 5°C per Myr after their intrusion at approximately 91.7 ± 0.3 Ma and 106.7 ± 0.4 Ma (shown by the pink lines in Fig. 18). All the shown histories are created using the methodology of Gallagher et al. (2009) and Gallagher (2012) and the diffusion and kinetic parameters used in the equations mentioned in Lee et al. (1997), Cherniak and Watson (2001) and Ullah et al. (2023a). Both areas show simple cooling histories with no major thermal event occurring above the closure temperatures of the Pb in zircons (Lee et al., 1997; Cherniak and Watson, 2001; Ullah et al., 2023a). The preservation of the ages of these intrusive units of 91.7 ± 0.3 Ma and 106.7 ± 0. 4 Ma suggests that the Pb diffusion had not experienced a major heating or remelting event afterward (Fig. 18). These observations are also in agreement with the available petrographic information

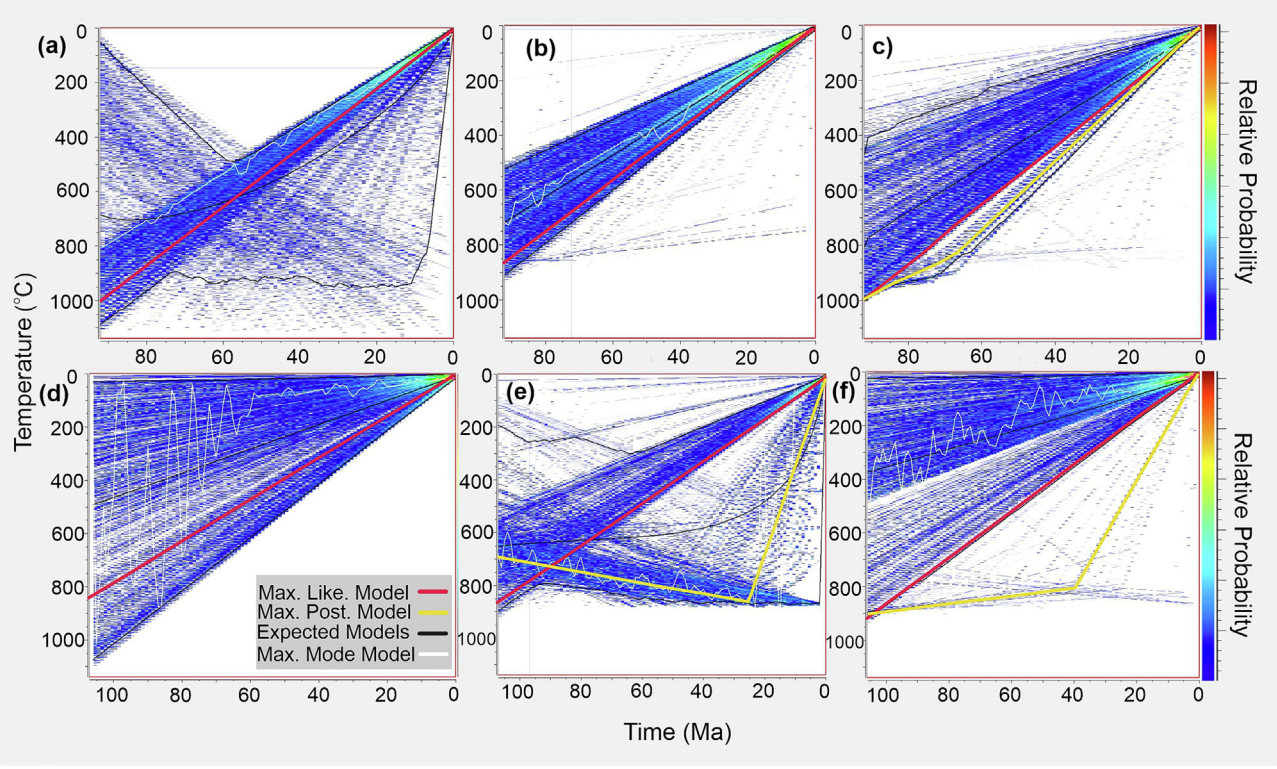

Fig.18. Thermal history models for the (a-c) the Kohistan batholith and (d-f) the Khunjerab pluton using the diffusion and kinetic parameters of Lee et al. (1997; b and e), Cherniak and Watson (2001; c and f), and Ullah et al. (2023a; a and d).

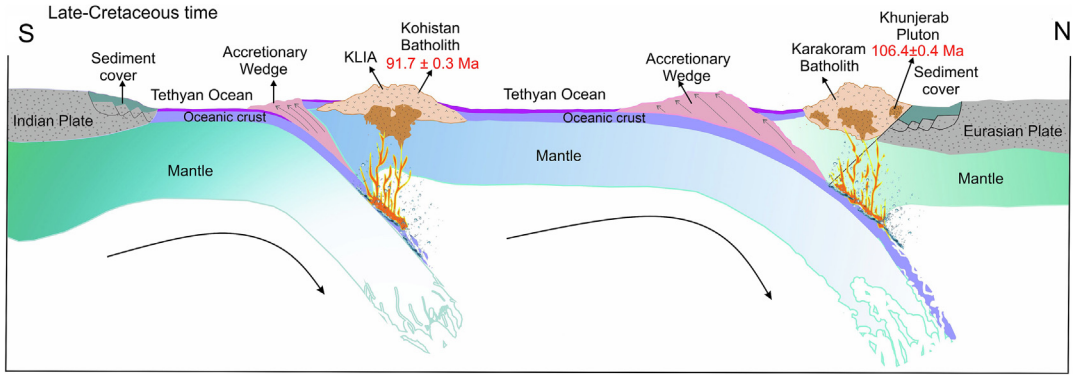

Fig.19. Conceptual tectonic setting model for the studied samples of the Kohistan and Khunjerab pluton summarizing all the analyses and literature review of this work.

(Fig. 2) and the CL images of these zircons which shows concentric oscillatory zoning with symmetric growth (Figs. 11-13).

5.6. Implication for the geodynamics of Indo-Eurasian crust

Two subduction processes drove significant tectonic activity in the Neo-Tethys Ocean, which was located between the Indian and Eurasian plates during the Jurassic to Late Cretaceous (Fig. 19). One was the intra-oceanic KLIA, which resulted from the Neo-Tethys Ocean subducting beneath the Meso-Tethys oceanic crust in a northerly direction. Concurrently, the same oceanic plate subducted beneath southern Eurasia to the north, creating the Karakoram block (Crawford and Searle, 1992; Fig. 19). However, little is known about the precise moment when the subduction-related magmatic activity in the KLIA began. According to Ali et al. (2024), the Matum-Das tonalite (U-Pb age of ca. 150 Ma) is important marker of the beginning of subduction-related volcanic activity in the KLIA. Also, according to Cao et al. (2016) and Saktura et al. (2021), the subduction related magmatism towards the Karakorum side starts at about 165 – 145 Ma. Furthermore, the results of geochemical analysis at both magmatic sides of the two subduction zones show that both the Kohistan batholith and the Khunjerab pluton samples show LILE enrichment indicating the effect of the slab-derived fluids from the subducting plate, indicating that the arc and the subduction were active at 91.7 Ma as the REE data shows the same pattern as that of the tonalite of Ali et al. (2024). Based on these geological and geochemical features, Neo-Tethys subduction at the two locations is thought to have started in the late Jurassic (i.e., in accordance with Ali et al. (2024) and Saktura et al. (2021)) and continued until the Late-Cretaceous (ca. 91.7 Ma) and Mid-Late-Cretaceous (ca. 106.4 Ma) in the Kohistan batholith and the Karakorum block (Khunjerab pluton) respectively. Contemporaneous or somewhat earlier volcanic activity in these regions is suggested by the dating of felsic rocks, such as granite (101 Ma) from the Gangdese pluton in Ladakh (Schärer et al., 1984) and igneous rocks (110 Ma) from the Central Lhasa subterrain in Tibet (Zhu et al., 2009, 2011) while the contemporaneous volcanic activity to Khunjerab pluton is that of Tirich Mir granite (dated at 115 Ma by Desio (1964) and 103 Ma by Villa et al. (2001)). This suggests that they were the component of the same subduction system that further evolved the crust of the Karakoram block and KLIA and all of these volcanic activities in both blocks were controlled by the northward subduction of the oceanic lithosphere of the Neo-Tethys.

The studied rocks of the Kohistan batholith share similar chemical characteristics with igneous rocks of the Lhasa Terrane, Tibet (Zhu et al., 2009) while samples of the Khunjerab pluton share similar characteristics with the Tirich Mir granitic plutons (Desio, 1964; Villa et al., 2001). In samples of the Kohistan batholith, the fractionation of the granitoids occurred at greater depth than in the Khunjerab pluton. These types of subductions typically occur close to the plate boundaries, where a relatively older, dense section of ocean floor is pushed beneath another relatively younger and less dense ocean floor (as in case of KLIA; Fig. 19) or a continent (as in case of Karakorum block or the Khunjerab pluton; Fig. 19). Both the Mid-Late Cretaceous magmatic events recorded in this study are distinct from each other in terms of mineralogy, ages, and geodynamic setting as the Khunjerab pluton was emplaced at shallower depth than the Kohistan batholith. Further, all of the above discussions disclose the different nature of partly coeval magmatism in both magmatic units, i.e., continental arc magmatism in the Karakoram block (ca. 106.4 Ma) and island-arc magmatism in the Kohistan-Ladakh region (ca. 91.7 Ma).

6. Conclusions

Study of the Mid-Late Cretaceous pre-collision magmatic units in the Kohistan batholith (located in KLIA) and the Khunjerab pluton (located in Karakoram block; Eurasian plate) allow several noteworthy conclusions based on petrographic, geochemical, TEM and geochronological data.

(1) The ages of the associated magmatic bodies of the Kohistan batholith and the Khunjerab pluton show magmatism and crystallization at different periods of time; the Kohistan batholith formed at 91.7 ± 0.3 Ma, almost 15 Ma earlier than the magmatic event (Khunjerab pluton) in the Karakoram or in the southern part of Eurasian plate, which formed at 106.4 ± 0.4 Ma. This indicates an independent emplacement of both units.

(2) This study also demonstrates the effect of chemical heterogeneity and metamictization on the U-Pb systematics of the magmatic zircon of both units and suggest a multi grain U-Pb dating of the zircon in magmatic rocks to improve analytical/geochemical accuracy.

(3) The integrated study of the whole rock geochemistry, chemical analysis of the hydrous minerals, and the thermal modelling suggest the magma sources of the Kohistan batholith and Khunjerab pluton are metasomatized mantle wedges above their respective subduction slabs.

(4) Despite different ages and mineralogy both units are distinct with respect to their origin and belong to different subduction settings with the Khunjerab pluton being emplaced at shallower depth than the Kohistan batholith.

CRediT authorship contribution statement

Matee Ullah: Writing – review & editing, Writing – original draft, Visualization, Validation, Methodology, Investigation, Formal

analysis, Data curation, Conceptualization. **Urs Klötzli:** Writing – review & editing, Funding acquisition. **Christian Rentenberger:** Methodology, Investigation. **Jiří Sláma:** Methodology, Investigation. **Muhammad Younas:** Visualization. **Muhammad Khubab:** Visualization. **Mohammad Goudarzi:** Visualization. **Tanveer Ahmad:** Writing – review & editing.

Declaration of competing interest

The authors declare that they have no known competing financial interests or personal relationships that could have appeared to influence the work reported in this paper.

Acknowledgments

This research work is published from the PhD work of the first author, funded by the Higher Education Commission of Pakistan under the Faculty Development Program for the Khushal Khan Khattak University, Karak, Pakistan with grant No. 386-388/PC/PAB/ KKKUK/21. Partial funds are provided by the University of Vienna, Austria. The Department of Lithospheric Research, and Physics of Nano Nanostructured Materials Laboratory, University of Vienna is also acknowledged for providing access to FIB-SEM, EPMA, TEM and different laboratories.

Appendix A. Supplementary data

Supplementary data to this article can be found online at https://doi.org/10.1016/j.gsf.2025.102003.

References

Abdel-Rahman, A.F.M., 1994. Nature of biotites from alkaline, calc-alkaline, and peraluminous magmas. J. Petrol. 35 (2), 525–541.
Alférez, G.H., Esteban, O.A., Clausen, B.L., Ardila, A.M.M., 2022. Automated machine learning pipeline for geochemical analysis. Earth Sci. Inform. 15 (3), 1683–1698.
Ali, M., Zhao, K.D., Wang, C., Rehman, H.U., Hussain, A., Mahar, M.A., Lutfi, W., 2024. Geochemical and isotopic constraints on the origin and evolution of the Matum-Das tonalite and mafic enclaves from the Kohistan Batholith, Northern Pakistan. Lithos 470-471 (1), 107535.
Allegre, C.J., Minster, J.F., 1978. Quantitative models of trace element behavior in magmatic processes. Earth Planet. Sci. Lett. 38 (1), 1–25.
Argles, T., Foster, G., Whittington, A., Harris, N., George, M., 2003. Isotope studies reveal a complete Himalayan section in the Nanga Parbat syntaxis. Geology 31 (12), 1109–1112.
Belousova, E.A., Griffin, W.L., O'Reilly, S.Y., Fisher, N.L., 2002. Igneous zircon: trace element composition as an indicator of source rock type. Contrib. Mineral. Petrol. 143, 602–622.
Bepler, T., Kelley, K., Noble, A.J., Berger, B., 2020. Topaz-Denoise: general deep denoising models for cryoEM and cryoET. Nat. Commun. 11 (1), 5208.
Boehnke, P., Watson, E.B., Trail, D., Harrison, T.M., Schmitt, A.K., 2013. Zircon saturation re-revisited. Chem. Geol. 351, 324–334.
Bohrson, W.A., Spera, F.J., Heinonen, J.S., Brown, G.A., Scruggs, M.A., Adams, J.V., Suikkanen, E., 2020. Diagnosing open-system magmatic processes using the Magma Chamber Simulator (MCS): part I—major elements and phase equilibria. Contrib. Mineral. Petrol. 175, 1–29.
Bosch, D., Garrido, C.J., Bruguier, O., Dhuime, B., Bodinier, J.L., Padròn-Navarta, J.A., Galland, B., 2011. Building an island-arc crustal section: time constraints from a LA-ICP-MS zircon study. Earth Planet. Sci. Lett. 309 (3–4), 268–279.
Cao, M., Qin, K., Li, G., Li, J., Zhao, J., Evans, N.J., Hollings, P., 2016. Tectono-magmatic evolution of Late Jurassic to Early Cretaceous granitoids in the west central Lhasa subterrane, Tibet. Gondwana Res. 39, 386–400.
Chappell, B.W., 1999. Aluminium saturation in I-and S-type granites and the characterization of fractionated haplogranites. Lithos 46 (3), 535–551.
Cherniak, D.J., Watson, E.B., 2001. Pb diffusion in zircon. Chem. Geol. 172 (1–2), 5–24.
Chiaradia, M., 2015. Crustal thickness control on Sr/Y signatures of recent arc magmas: an Earth scale perspective. Sci. Reports 5 (1), 8115.
Chilson-Parks, B.H., Calabozo, F.M., Saal, A.E., Wang, Z., Mallick, S., Petrinovic, I.A., Frey, F.A., 2022. The signature of metasomatized subcontinental lithospheric mantle in the basaltic magmatism of the Payenia volcanic province, Argentina. Geochem. Geophys. Geosys. 23 (1), e2021GC010071.
Crawford, M.B., Searle, M.P., 1992. Field relationships and geochemistry of pre-collisional (India-Asia) granitoid magmatism in the central Karakoram, northern Pakistan. Tectonophysics 206 (1–2), 171–192.
Debon, F., Ali Khan, N., 1996. Alkaline orogenic plutonism in the Karakorum batholith: the Upper Cretaceous Koz Sar complex (Karambar valley, N. Pakistan). Geodinamica Acta 9 (4), 145–160.
Desio, A., 1964. On the geological ages of some granites of the Karakoram-Hindukush and Badakhashan (Central Asia). In 22nd International Geological Congress, Vol. 11, pp. 479-496.
Djimbi, D.M., Gautheron, C., Roques, J., Tassan-Got, L., Gerin, C., Simoni, E., 2015. Impact of apatite chemical composition on (U-Th)/He thermochronometry: An atomistic point of view. Geochim. Cosmochim. Acta 167, 162–176.
Ewing, R.C., Meldrum, A., Wang, L., Weber, W.J., Corrales, L.R., 2003. Radiation effects in zircon. Rev. Mineral. Geochem. 53 (1), 387–425.
Foster, M.D., 1960. Interpretation of the composition of trioctahedral mica. U.S. Geological Survey Professional Paper, v. 354-B, pp. 11–48.
Frost, B.R., Barnes, C.G., Collins, W.J., Arculus, R.J., Ellis, D.J., Frost, C.D., 2001. A geochemical classification for granitic rocks. J. Petrol. 42 (11), 2033–2048.
Gallagher, K., 2012. Transdimensional inverse thermal history modeling for quantitative thermochronology. J. Geophy. Res. Solid Earth 117 (B2), e2021GC010071.
Gallagher, K., Charvin, K., Nielsen, S., Sambridge, M., Stephenson, J., 2009. Markov chain Monte Carlo (MCMC) sampling methods to determine optimal models, model resolution and model choice for Earth Science problems. Marine Petrol. Geol. 26 (4), 525–535.
Gao, P., Zheng, Y.F., Zhao, Z.F., 2016. Distinction between S-type and peraluminous I-type granites: Zircon versus whole-rock geochemistry. Lithos 258, 77–91.
Gautheron, C., Djimbi, D.M., Roques, J., Balout, H., Ketcham, R.A., Simoni, E., Tassan-Got, L., 2020. A multi-method, multi-scale theoretical study of He and Ne diffusion in zircon. Geochim. Cosmochim. Acta 268, 348–367.
Giambiagi, L., Mescua, J., Bechis, F., Tassara, A., Hoke, G., 2012. Thrust belts of the southern Central Andes: Along-strike variations in shortening, topography, crustal geometry, and denudation. Bulletin 124(7-8), 1339-1351.
Grove, T.L., Donnelly-Nolan, J.M., Housh, T., 1997. Magmatic processes that generated the rhyolite of Glass Mountain, Medicine Lake volcano, Northern California. Contrib. Mineral. Petrol. 127, 205–223.
Grove, T.L., Elkins-Tanton, L.T., Parman, S.W., Chatterjee, N., Müntener, O., Gaetani, G.A., 2003. Fractional crystallization and mantle-melting controls on calc-alkaline differentiation trends. Contrib. Mineral. Petrol. 145, 515–533.
Hartman, J., Franks, R., Gehrels, G., Hourigan, J., Wenig, P., 2017. Decoding Data Files from a Thermo Element TM ICP Mass Spectrometer, 15 pp. Manual available online at https://github.com/jhh67/extractdat.git [15.10. 2019].
Gualda, G.A., Ghiorso, M.S., 2015. MELTS _ E xcel: AM icrosoft E xcel-based MELTS interface for research and teaching of magma properties and evolution. Geochem. Geophys. Geosys. 16 (1), 315–324.
Gualda, G.A., Ghiorso, M.S., Lemons, R.V., Carley, T.L., 2012. Rhyolite-MELTS: a modified calibration of MELTS optimized for silica-rich, fluid-bearing magmatic systems. J. Petrol. 53 (5), 875–890.
Hawkesworth, C.J., Norry, M.J., Roddick, J.C., Vollmer, R., 1979. $^{143}Nd/^{144}Nd$ and $^{87}Sr/^{86}Sr$ ratios from the Azores and their significance in LIL-element enriched mantle. Nature 280 (5717), 28–31.
Heinonen, J.S., Bohrson, W.A., Spera, F.J., Brown, G.A., Scruggs, M.A., Adams, J.V., 2020. Diagnosing open-system magmatic processes using the Magma Chamber Simulator (MCS): part II—trace elements and isotopes. Contrib. Mineral. Petrol. 175, 1–21.
Henry, D.J., Guidotti, C.V., Thomson, J.A., 2005. The Ti-saturation surface for low-to-medium pressure metapelitic biotites: Implications for geothermometry and Ti-substitution mechanisms. Am. Mineralogist 90 (2–3), 316–328.
Hermann, J., 2002. Allanite: thorium and light rare earth element carrier in subducted crust. Chem. Geol. 192 (3–4), 289–306.
Heuberger, S., Schaltegger, U., Burg, J.P., Villa, I.M., Frank, M., Dawood, H., Zanchi, A., 2007. Age and isotopic constraints on magmatism along the Karakoram-Kohistan Suture Zone, NW Pakistan: Evidence for subduction and continued convergence after India-Asia collision. Swiss J. Geosci. 100, 85–107.
Hildebrand, P.R., Noble, S.R., Searle, M.P., Waters, D.J., Parrish, R.R., 2001. Old origin for an active mountain range: Geology and geochronology of the eastern Hindu Kush, Pakistan. Geol. Soc. Am. Bull. 113 (5), 625–639.
Hirschmann, M.M., Ghiorso, M.S., Davis, F.A., Gordon, S.M., Mukherjee, S., Grove, T.L., Till, C.B., 2008. Library of Experimental Phase Relations (LEPR): A database and Web portal for experimental magmatic phase equilibria data. Geochem. Geophys. Geosys. 9, 3.
Honegger, K., Dietrich, V., Frank, W., Gansser, A., Thöni, M., Trommsdorff, V., 1982. Magmatism and metamorphism in the Ladakh Himalayas (the Indus-Tsangpo suture zone). Earth Planet. Sci. Lett. 60 (2), 253–292.
Hönig, S., Čopjaková, R., Škoda, R., Novák, M., Dolejš, D., Leichmann, J., Galiová, M.V., 2014. Garnet as a major carrier of the Y and REE in the granitic rocks: An example from the layered anorogenic granite in the Brno Batholith, Czech Republic. Am. Mineral. 99 (10), 1922–1941.
Horstwood, M.S., Košler, J., Gehrels, G., Jackson, S.E., McLean, N.M., Paton, C., Schoene, B., 2016. Community-derived standards for LA-ICP-MS U-(Th-) Pb geochronology–Uncertainty propagation, age interpretation and data reporting. Geostand. Geoanalyt. Res. 40 (3), 311–332.
Irvine, T.N., Baragar, W.R.A.F., 1971. A guide to the chemical classification of the common volcanic rocks. Can. J. Earth Sci. 8 (5), 523–548.

Jackson, S.E., Pearson, N.J., Griffin, W.L., Belousova, E.A., 2004. The application of laser ablation-inductively coupled plasma-mass spectrometry to in situ U–Pb zircon geochronology. Chem. Geol. 211 (1–2), 47–69.
Jagoutz, O., Bouilhol, P., Schaltegger, U., Müntener, O., 2019. The isotopic evolution of the Kohistan Ladakh arc from subduction initiation to continent arc collision. Geol. Soc. London Special Pub. 483 (1), 165–182.
Jagoutz, O.E., Burg, J.P., Hussain, S., Dawood, H., Pettke, T., Iizuka, T., Maruyama, S., 2009. Construction of the granitoid crust of an island arc part I: geochronological and geochemical constraints from the plutonic Kohistan (NW Pakistan). Contrib. Mineral. Petrol. 158, 739–755.
Khan, S.D., Walker, D.J., Hall, S.A., Burke, K.C., Shah, M.T., Stockli, L., 2009. Did the Kohistan-Ladakh island arc collide first with India? Geol. Soc. Am. Bull. 121 (3–4), 366–384.
Krol, M.A., Zeitler, P.K., Poupeau, G., Pecher, A., 1996. Temporal variations in the cooling and denudation history of the Hunza plutonic complex, Karakoram Batholith, revealed by $^{40}Ar/^{39}Ar$ thermochronology. Tectonics 15 (2), 403–415.
Kudo, A.M., Weill, D.F., 1970. An igneous plagioclase thermometer. Contrib. Mineral. Petrol. 25 (1), 52–65.
Kusiak, M.A., Dunkley, D.J., Wirth, R., Whitehouse, M.J., Wilde, S.A., Marquardt, K., 2015. Metallic lead nanospheres discovered in ancient zircons. Proc. Nation. Aca. Sci. 112 (16), 4958–4963.
Lee, J.K., Williams, I.S., Ellis, D.J., 1997. Pb, U and Th diffusion in natural zircon. Nature 390 (6656), 159–162.
McDonough, W.F., Sun, S.S., 1995. The composition of the Earth. Chem. Geol. 120 (3–4), 223–253.
Middlemost, E.A., 1994. Naming materials in the magma/igneous rock system. Earth Sci. Rev. 37 (3–4), 215–224.
Nachit, H., Ibhi, A., Ohoud, M.B., 2005. Discrimination between primary magmatic biotites, re-equilibrated biotites and neo-formed biotites. Comptes Rendus Géoscience 337 (16), 1415–1420.
Noda, A., 2017. A new tool for calculation and visualization of U–Pb age data: UPbplot. py. Bull. Geol. Survey Japan 68 (3), 131–140.
Ogasawara, M., Khan, T., Khan, F., Kito, N., Morishita, Y., 2008. Ion microprobe U-Pb ages of the Khunjerab granodiorite and some granitoids from Karakoram. Pakistan. Himalayan J. Sci. 2 (4), 212.
Ogasawara, M., Watanabe, Y., Khan, F., Khan, T., Khan, M.S.Z., Khan, S.A., 1992. Late Cretaceous igneous activity and tectonism of the Karakoram block in the Khunjerab Valley, Northern Pakistan. In geology in South Asia-i. Proceedings of the First South Asia Geological Congress.
Paton, C., Hellstrom, J., Paul, B., Woodhead, J., Hergt, J., 2011. Iolite: Freeware for the visualisation and processing of mass spectrometric data. J. Analyt. Atomic Spectrom. 26 (12), 2508–2518.
Pearce, J.A., Harris, N.B., Tindle, A.G., 1984. Trace element discrimination diagrams for the tectonic interpretation of granitic rocks. J. Petrol. 25 (4), 956–983.
Petrus, J.A., Kamber, B.S., 2012. VizualAge: A novel approach to laser ablation ICP-MS U-Pb geochronology data reduction. Geostand. Geoanalyt. Res. 36 (3), 247–270.
Petterson, M.G., 2010. A review of the geology and tectonics of the Kohistan Island arc, north Pakistan. Geol. Soc. London Special Pub. 338 (1), 287–327.
Petterson, M.G., Windley, B.F., 1985. Rb-Sr dating of the Kohistan arc-batholith in the Trans-Himalaya of north Pakistan, and tectonic implications. Earth Planet. Sci. Lett. 74 (1), 45–57.
Petterson, M.G., Windley, B.F., 1991. Changing source regions of magmas and crustal growth in the Trans-Himalayas: evidence from the Chalt volcanics and Kohistan batholith, Kohistan, northern Pakistan. Earth Planet. Sci. Lett. 102 (3–4), 326–341.
Reichardt, H., Weinberg, R.F., Andersson, U.B., Fanning, C.M., 2010. Hybridization of granitic magmas in the source: the origin of the Karakoram Batholith, Ladakh, NW India. Lithos 116 (3–4), 249–272.
Ridolfi, F., 2021. Amp-TB2: An updated model for calcic amphibole thermobarometry. Minerals 11, 324.
Saktura, W.M., Buckman, S., Nutman, A.P., Bennett, V.C., 2021. Late Jurassic Changmar complex from the Shyok ophiolite, NW Himalaya: A prelude to the Ladakh arc. Geol. Mag. 158 (2), 239–260.
Schaltegger, U., Zeilinger, G., Frank, M., Burg, J.P., 2002. Multiple mantle sources during island arc magmatism: U–Pb and Hf isotopic evidence from the Kohistan arc complex, Pakistan. Terra Nova 14 (6), 461–468.
Schärer, U., Hamet, J., Allègre, C.J., 1984. The Trans-Himalaya (Gangdese) plutonism in the Ladakh region: a U-Pb and Rb-Sr study. Earth Planet. Sci. Lett. 67 (3), 327–339.
Searle, M.P., Khan, M.A., Fraser, J.E., Gough, S.J., Jan, M.Q., 1999. The tectonic evolution of the Kohistan-Karakoram collision belt along the Karakoram Highway transect, north Pakistan. Tectonics 18 (6), 929–949.
Sheffels, B.M., 1990. Lower bound on the amount of crustal shortening, in the central Bolivian Andes. Geology 18 (9), 812–815.
Shellnutt, J.G., 2018. Derivation of intermediate to silicic magma from the basalt analyzed at the Vega 2 landing site, Venus. Plos One 13 (3), e0194155.
Sláma, J., Košler, J., Condon, D.J., Crowley, J.L., Gerdes, A., Hanchar, J.M., Whitehouse, M.J., 2008. Plešovice zircon—a new natural reference material for U–Pb and Hf isotopic microanalysis. Chem. Geol. 249 (1–2), 1–35.
Smith, D.J., 2014. Clinopyroxene precursors to amphibole sponge in arc crust. Nat. Commun. 5 (1), 4329.
Sun, S.S., McDonough, W.F., 1989. Chemical and isotopic systematics of oceanic basalts: implications for mantle composition and processes. Geol. Soc. London Special Pub. 42 (1), 313–345.
Tatsumi, Y., 2005. The subduction factory: How it operates in the evolving Earth. GSA Today 15 (7), 4.
Tischendorf, G., Gottesmann, B., Förster, H.J., Trumbull, R.B., 1997. On Li-bearing micas: estimating Li from electron microprobe analyses and an improved diagram for graphical representation. Mineral. Mag. 61 (409), 809–834.
Tramm, F., Wirth, R., Budzyń, B., Sláma, J., Schreiber, A., 2021. LA-ICP-MS and TEM constraints on the magmatic and post-magmatic processes recorded by the zircon-xenotime intergrowth in pegmatite (Piława Górna, Góry Sowie Block, SW Poland). Lithos 404, 106480.
Treloar, P.J., Rex, D.C., Guise, P.G., Coward, M.P., Searle, M.P., Windley, B.F., Luff, I.W., 1989. K-Ar and Ar-Ar geochronology of the Himalayan collision in NW Pakistan: Constraints on the timing of suturing, deformation, metamorphism and uplift. Tectonics 8 (4), 881–909.
Tunheng, A., Hirata, T., 2004. Development of signal smoothing device for precise elemental analysis using laser ablation-ICP-mass spectrometry. J. Anal. Atomic Spectrom. 19 (7), 932–934.
Ullah, M., Klötzli, U., Wadood, B., Khubab, M., Islam, F., Shehzad, K., Ahmad, R., 2023a. Pb diffusion in perfect and defective zircon for thermo/petro-chronological investigations: An atomistic approach. Chem. Geol. 640, 121750.
Ullah, M., Klötzli, U., Tassan-Got, L., Islam, F., Younas, M., Shehzad, K., Wadood, B., 2023b. Effect of heterogeneity on the diffusion of Pb in apatite for petrochronological applications: A multiscale approach to characterizing the influence of apatite chemistry and anisotropy on Pb diffusion. Lithos 460, 107396.
Ulmer, P., 2001. Partial melting in the mantle wedge—the role of H_2O in the genesis of mantle-derived 'arc-related'magmas. Phys. Earth Planet. Inter. 127 (1–4), 215–232.
Vermeesch, P., 2018. IsoplotR: A free and open toolbox for geochronology. Geosci. Front. 9 (5), 1479–1493.
Villa, I.M., Hanchar, J.M., 2017. Age discordance and mineralogy. Am. Mineral. 102 (12), 2422–2439.
Villa, I., Zanchi, A., Gaetani, M., 2001. Rb-Sr dating of the Tirich Mir pluton, NW Pakistan: pre-140 Ma accretion of the Karakoram terrane to the Asian margin. J. Asian Earth Sci. 19 (3A), 72.
Vonlanthen, P., Gerald, J.D.F., Rubatto, D., Hermann, J., 2012. Recrystallization rims in zircon (Valle d'Arbedo, Switzerland): An integrated cathodoluminescence, LA-ICP-MS, SHRIMP, and TEM study. Am. Mineral. 97 (2–3), 369–377.
Whalen, J.B., Currie, K.L., Chappell, B.W., 1987. A-type granites: geochemical characteristics, discrimination and petrogenesis. Contrib. Mineral. Petrol. 95, 407–419.
Wiedenbeck, M.A.P.C., Alle, P., Corfu, F.Y., Griffin, W.L., Meier, M., Oberli, F.V., Spiegel, W., 1995. Three natural zircon standards for U-Th-Pb, Lu-Hf, trace element and REE analyses. Geostandards Newslett. 19 (1), 1–23.
Wigger, P.J., Schmitz, M., Araneda, M., Asch, G., Baldzuhn, S., Giese, P., Viramonte, J., 1994. In: Variation in the Crustal Structure of the Southern Central Andes Deduced from Seismic Refraction Investigations. Springer, Berlin, pp. 23–48.
Wirth, R., 2009. Focused Ion Beam (FIB) combined with SEM and TEM: Advanced analytical tools for studies of chemical composition, microstructure and crystal structure in geomaterials on a nanometre scale. Chem. Geol. 261 (3–4), 217–229.
Wolf, M.B., London, D., 1994. Apatite dissolution into peraluminous haplogranitic melts: an experimental study of solubilities and mechanisms. Geochim. Cosmoch. Acta 58 (19), 4127–4145.
Wones, D.R., 1989. Significance of the assemblage titanite+ magnetite+ quartz in granitic rocks. Am. Mineral. 74 (7–8), 744–749.
Wu, H., Xie, C., Li, C., Wang, M., Fan, J., Xu, W., 2016. Tectonic shortening and crustal thickening in subduction zones: Evidence from Middle–Late Jurassic magmatism in Southern Qiangtang, China. Gondwana Res. 39, 1–13.
Zhu, D.C., Mo, X.X., Niu, Y., Zhao, Z.D., Wang, L.Q., Liu, Y.S., Wu, F.Y., 2009. Geochemical investigation of Early Cretaceous igneous rocks along an east–west traverse throughout the central Lhasa Terrane, Tibet. Chem. Geol. 268 (3–4), 298–312.
Zhu, D.C., Zhao, Z.D., Niu, Y., Mo, X.X., Chung, S.L., Hou, Z.Q., Wu, F.Y., 2011. The Lhasa Terrane: Record of a microcontinent and its histories of drift and growth. Earth Planet. Sci. Lett. 301 (1–2), 241–255.